Materialia 21 (2022) 101350

Contents lists available at ScienceDirect

Materialia

journal homepage: www.elsevier.com/locate/mtla

Full Length Article

Determination of the friction stir welding window from the solid-state-bonding mechanics under severe thermomechanical conditions☆

Xue Wang[a], Yanfei Gao[a,*], Martin McDonnell[b], Zhili Feng[c,*]

[a] Department of Materials Science and Engineering, University of Tennessee, Knoxville, TN 37996, USA
[b] US Army DEVCOM Ground Vehicle Systems Center, Warren, MI 48397, USA
[c] Materials Science and Technology Division, Oak Ridge National Laboratory, Oak Ridge, TN 37831, USA

ARTICLE INFO

Keywords:
friction stir welding
Interfacial stick-slip condition
Solid state bonding
Interfacial cavity shrinkage
Needleman-Rice length scale
Processing window

ABSTRACT

The vast literature and industrial standards state that most solid-state bonding techniques, particularly the diffusion bonding, are mainly governed first by the plastic crushing of rough surface asperities, and then by volumetric inter-diffusion that eliminate the interfacial pores. We shall demonstrate that the first stage plays an insignificant role and the second one is not relevant at all. In this work, first, we note that the evolution of interfacial cavities (or pores, voids, etc.) under applied thermomechanical loading histories is a reverse process of the high-temperature creep fracture of polycrystalline materials by grain-boundary cavities. The well-established knowledge in the latter suggests that the interfacial cavity evolution be governed by the Needleman-Rice length scale, dictated from the comparison between a lateral diffusive process on the bonded interface and the creep deformation. In this regard, we derive a general modeling framework of bonding fraction evolution, which directly depends on the stress, strain rate, and temperature fields near the interface. Second, the above bonding model is applied to the Friction Stir Welding (FSW) process. The full field information from our prior simulations is used as inputs to assess the evolution and extent of bonding fraction at the workpiece-workpiece interface. Based on the stick-slip contact analysis, an approximate but analytical solution has been developed to derive the bonding fraction field, and the predicted ultimate bonding extent with respect to these parameters becomes a figure of merit for the study of processing window for industrial applications and design of the FSW process.

1. Introduction

Welding and joining of various components into a strong, durable and cost-effective engineering structure is a critical process in many industrial applications. The conventional fusion welding may reduce the stress concentration and common fatigue intolerance problem that introduced by fastening and riveting, but the related high temperature could dramatically change the microstructure of the base material and therefore lead to the weakest links for premature failure. In order to overcome these drawbacks in fusion welding, there exists a wide range of solid-state bonding techniques, such as diffusion bonding where workpieces are held by compressive force at elevated temperature [1,2], frictional bonding where two abutting workpieces slide against each other for heat generation [3], ultrasonic welding [4,5], impact or explosive welding [6,7], and friction stir welding (FSW) where a spinning and traversing tool onto two workpieces in butt configuration generates significant heat and deformation field [8,9]. Impact welding is motivated from the accidental finding during World War I that pieces of shrapnel were found to weld to the target armor plates, when these two metallic materials collided under high strain rate. In friction-based welding techniques, heat is generated from both mechanical friction and severe plastic deformation. Diffusion bonding derives its name from the belief that interdiffusion across the two workpieces will promote the formation of atomic bonding. Because of no melting and solidification processes involved in the above solid-state bonding techniques, the resulting products could be immune from defect generation and property deterioration such as solidification cracking and unwanted microstructural evolution.

☆ This manuscript has been co-authored by UT-Battelle, LLC, under contract DE-AC05–00OR22725 with the US Department of Energy (DOE). The US government retains and the publisher, by accepting the article for publication, acknowledges that the US government retains a nonexclusive, paid-up, irrevocable, worldwide license to publish or reproduce the published form of this manuscript, or allow others to do so, for US government purposes. DOE will provide public access to these results of federally sponsored research in accordance with the DOE Public Access Plan (http://energy.gov/downloads/doe-public-access-plan).

* Corresponding authors.
E-mail addresses: ygao7@utk.edu (Y. Gao), fengz@ornl.gov (Z. Feng).

https://doi.org/10.1016/j.mtla.2022.101350
Received 29 September 2021; Accepted 29 January 2022
Available online 30 January 2022

Here we focus on the fundamental understanding of one important figure of merit in FSW applications, namely, predicting the extent and quality of the workpiece-workpiece bonding from processing conditions. To attain such an objective, we first need to understand the dependence of torque and total heat generation ratio on the processing, geometric, and material constitutive parameters, which has been shown to be critically dictated by the interfacial stick-slip condition on the tool-workpiece interface in our prior numerical and theoretical analyses [10–12]. These results will be used subsequently in this work as prerequisites for modeling the bonding evolution. A predictive bonding model should be able to assess various candidate mechanisms and identify the leading one with respect to the given temperature and strain rate field. Besides, by integrating the processing analysis and the bonding model, we aim to provide a concise and convenient way for application engineers to correlate the process, geometric, and material constitutive parameters to the bonding extent, so as to provide the design capabilities and the process window.

When brought into contact, any two metallic materials will not immediately bond together unless they are atomically smooth and contamination free, i.e., “crack healing” does not happen in realistic conditions. In the cold welding experiment by Lu et al. [13], two ultrathin gold nanowires were brought to contact in their ends, but the mating surfaces are at most atomistically faceted/ledged and thus essentially flat. Such successes hardly exist for large objects. Adhesive forces of the long-range nature, such as van der Waals interaction or capillary force, cannot deform roughness asperities sufficiently for contact conformity because of the high stiffness of metallic materials. Naturally, it is anticipated that the solid-state bonding will be achieved at high compressive loads and high temperatures. It is therefore often believed that the bonding mechanisms include two stages [1–3,14]: (1) plastic crushing of rough surface asperities under an applied load which establishes an initial contact with a high fraction of true contact area, and (2) atomic interdiffusion by which atoms transport across the workpiece interface and promote the gap closure. Gould [15] emphasizes the critical roles of thermal dissolution of oxides and contaminants, realignment of the grain structures for bonding, and breakdown of the interfacial structure, among many other factors. These are certainly critical issues but are beyond the scope of this work. In Hamilton [16] and Chen et al. [17], surface roughness is regarded as a succession of extended ridges or asperities, which are deemed to be flattened by the plastic deformation under pressure. However, rough surface contacts, as schematically illustrated in Fig. 1(a), are usually manifested microscopically by a small number of widely separated asperities per unit area. Even if a multi-affine or fractal roughness is considered (simply speaking, fine asperities on top of coarse asperities), the full plastic solutions [18] suggest that the lateral interactions of neighboring asperities and the additional compliance onto fine asperity contacts from the coarse asperity scale make it extremely difficult to realize a high fraction of true contact area. Besides, any theoretical model along this line suffers the same problem of ill-posedness of roughness characterization due to the fractal nature, so the connection between the rough surface contact analysis and the bonding evolution remains largely qualitative [19]. As will be shown later in this work, we believe that it is futile to dwell on the rough surface contact, because the majority time spent in the bonding evolution is on the creep-dominated cavity closure while different degrees of surface roughness play a negligible role. Creep solutions are typically very different from fully plastic deformation fields.

The bonding evolution at a slightly later stage can be regarded as the closure of interfacial cavities, which might be long, serpentine and connected, or isolated, as schematically illustrated in Fig. 1(b). Earlier works in the solid state bonding suggest the removal of these cavities by volumetric inter-diffusion between the two workpieces, so that Fick’s solutions for diffusion couple can be adopted. However, this cannot be the dominant mechanism unless at extremely high temperature, because the activation energy for diffusion ranks from high to low for volumetric, interface, and surface diffusion. At the moderate temperature range in most solid-state bonding techniques, cavity surface diffusion is essentially infinite and bulk diffusion is essentially zero when compared to interface diffusion. Derby and Wallach [20,21] proposed the interface energy reduction as in the sintering process and the applied joining pressure as the driving forces for the cavity closure, and later Hill and Wallach [22] added plastic deformation in the cavity junctions to these sintering-like analyses. Similarly, Guo and Ridley [23] divided the diffusional bonding processes into three subprocesses, which involved volume and interfacial diffusion coupled with creep, rigid collapse, and surface diffusion. It should be noted that all these solutions are from powder sintering, so that cavities are assumed to be closely spaced and the cavity junctions are treated as necks in their plastic deformation analysis. The actual creep deformation field in widely separated cavities will be otherwise different. Many solid-state bonding techniques are very fast, so that the contribution of diffusional processes might be limited. It remains rather unclear from these analyses on the competition between diffusional and creep processes. Additionally, Buffa et al. [24] presented the pressure-time and the pressure-time-flow criteria, by integrating the ratio of pressure and flow strength over the entire course of processing. However, they only interpreted their criteria as “equivalent time” and “equivalent length”, but did not offer a detailed physical scenario on how bonding is formed.

In this work, we propose a novel view on the solid state bonding by treating the bonding process as a reverse one to the intergranular fracture in polycrystalline materials. The latter has been well understood in a vast number of literature (e.g., [25–30] and references therein). At moderate temperature and stress, the dominant mechanisms include diffusive and creep-driven growth of grain boundary cavities, and these solutions can be used with some modifications for our cavity shrinkage problem. This viewpoint has many noteworthy differences from the conventional solid-state-bonding models. *First*, the mere consideration of interface energy reduction for the diffusive shrinkage of cavities is insufficient. In the classic Hull-Rimmer model [31], the applied stress field biases the chemical potential and thus drives the self-diffusion as described onto the third cavity in Fig. 1(c). Compression increases chemical potential while tension decreases it, and the resulting diffusion is *along* the bonded interface, as opposed to the widely accepted model of volumetric inter-diffusion in the direction *normal* to the interface. *Second*, creep deformation of the surrounding workpiece materials also contributes to the volume change of the cavity, as shown schematically by the first cavity in Fig. 1(c). The competition between interface diffusion and bulk creep determines a length scale, according to Needleman and Rice [32]. If this Needleman-Rice length is larger than the cavity size, then the cavity growth/shrinkage is governed by diffusive process; the opposite limit corresponds to the creep dominant behavior. Consequently, a complete understanding of bonding mechanisms requires a thorough knowledge of the applied thermomechanical trajectories for this Needleman-Rice-type analysis. Our preliminary calculations for FSW processes have been given in [33]. *Third*, as individual cavities are subjected to different thermomechanical loading histories, it is not amenable to track all these cavities in a discrete manner. As shown in Fig. 1(c), we can homogenize these cavities and design an order parameter field as proposed by Tvergaard [27]. All the above details needed for the establishment of our bonding model will be elaborated in Section 2.

For the FSW process, most literature studies on the effects of operation parameters on final bonding quality of the end products are mainly experimental and empirical. The most widely investigated parameters include the tool rotational speed, welding speed, and axial force. It has been found that the increase in rotational speed is favorable for enhancing joint strength [34–36]. Shen et al. [37] found that a higher penetration depth over a wide range of traveling speeds helps increase the weld strength. For the tool geometry, Boz and Kurt [38] and Zhao et al. [39] found that an improved bonding performance could be obtained using screw-pitched and tapered sir pin. However, numerical and analytical investigations on how these operation parameters affect the final

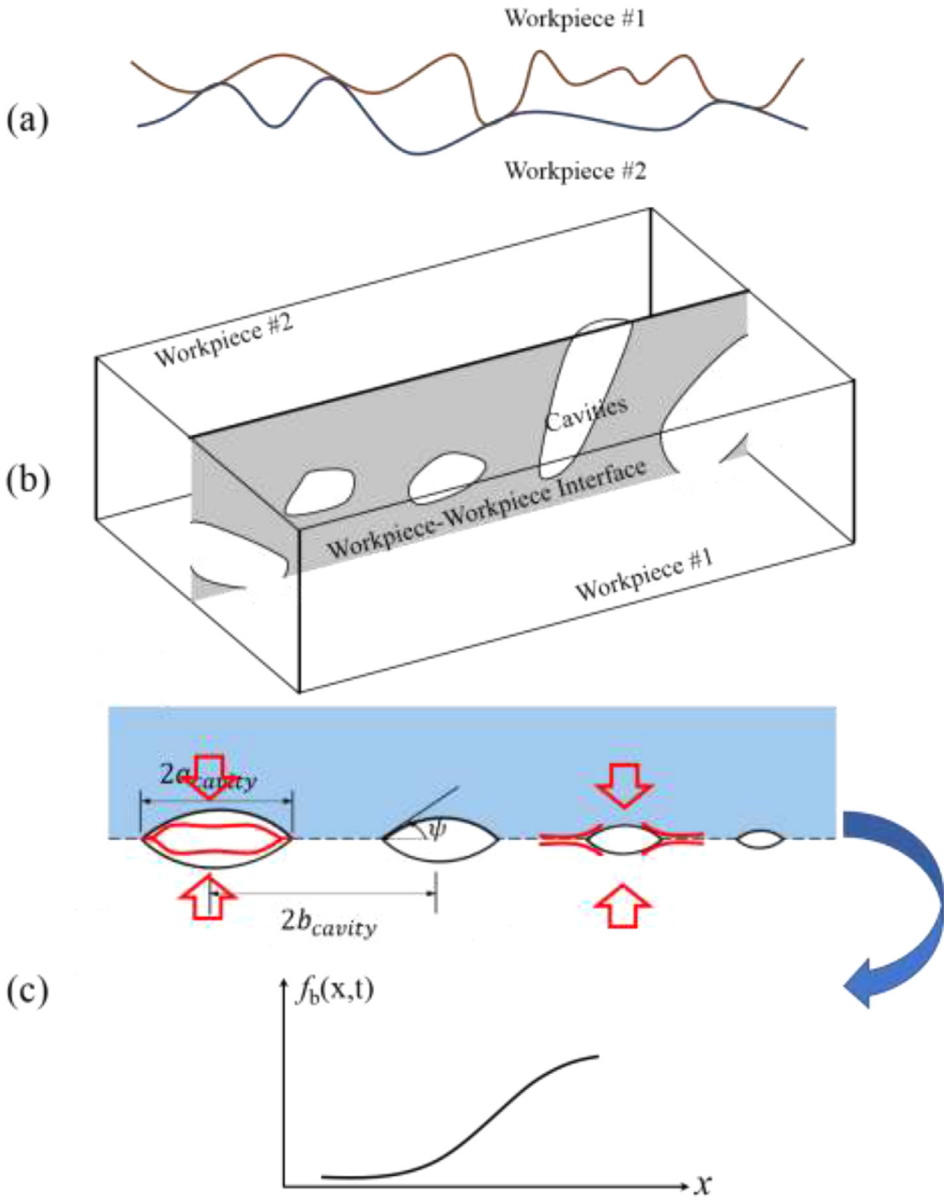

Fig. 1. Schematic illustration of various solid-state-bonding models. (a) Rough surface contact between two workpieces is usually supported by isolated and widely separated asperities. (b) Bonding two workpieces is equivalent to the shrinkage and closure of interfacial cavities. (c) A discrete array of cavities, which can be closed by creep-controlled or diffusive processes, is homogenized into a field of bonding fraction, $f_b(x_a, t)$.

bonding condition at interface is still limited. In our recent works [10–12], the relationship between these fields and the processing, geometric, material constitutive parameters has been thoroughly investigated, and an analytical solution based on the interfacial stick-slip behavior has been proposed and the predicted torque and total heat generation rate agree well with the numerical simulations. Because our bonding model in Section 2 depends directly on the temperature, strain rate, and stress fields and their histories, numerical simulation results of the FSW process will be directly used to predict the evolution of workpiece-workpiece bonding fraction with respect to varying input parameters, as will be presented in Section 3.

With so many controlling parameters involved in the FSW process, a better strategy that can find great applications in realistic problems will be the development of an analytical solution to predict the ultimate bonding extent. Our recent work [12] has developed an analytical solution to determine the dependence of torque and total heat generation rate on the interfacial stick-slip condition, which can be further extended to predict the full strain-rate and temperature fields. Combining these results with our findings in Sections 2 and 3, a flowchart of successive steps is proposed to first use the processing, geometric, and material constitutive parameters as input to determine the peak temperature and the stick-slip ratio, and then to use the resulting strain-rate field to determine the extent of full bonding, as will be explained in details in Section 4. When comparing the prediction from this analytical approach to the numerical simulation results in Section 3, we can identify the most critical input parameters, together with their ranges to which the final bonding extent is sensitive. These comparisons will be made for both FSW and friction stir cladding problem. A process window can be established from the finding that the bonding extent changes rapidly when traversing in the map of major processing parameters, as will be discussed in Section 5.

2. The solid-state bonding model

Referring to the processes in Fig. 1(c), we will first discuss the behavior of individual cavities under various closure mechanisms (top figure), and then formulate the homogenized model that can be readily used with finite element simulations (bottom figure).

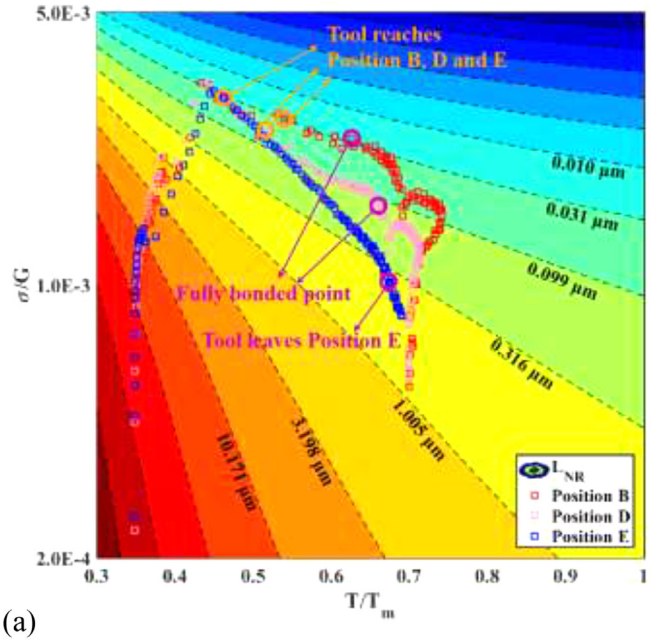

(a)

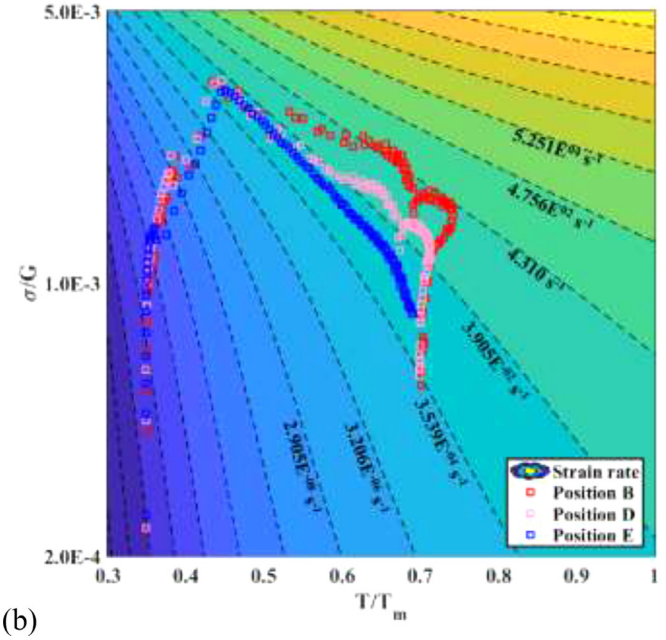

(b)

Fig. 2. (a) The contour plot of the Needleman-Rice length scale, L_{NR}, with respect to the homologous temperature and normalized stress, which dictates the relative significance of diffusive and creep-controlled processes for cavity closure. (b) The corresponding contour plot of strain rates for AA6061-T6 aluminum alloy. Overlaid on these plots are the thermomechanical histories of three reference points (B, D, and E) from Fig. 3(b). The orange markers denote the instant of tool front reaching these points, and the purple ones denote the condition of reaching full bonding for B and D and the condition of tool leaving point E.

The interfacial cavities are of the lenticular shape, and the half dihedral angle is determined from the Young-Dupré equation,

$$\cos\psi = \frac{\gamma_{interface}}{2\gamma_{cavity}} < 1, \tag{1}$$

where $\gamma_{interface}$ is the workpiece-workpiece interface energy per unit area, and γ_{cavity} is the cavity surface energy per unit area. The Laplace pressure inside the cavity modifies its chemical potential by

$$\Delta\mu_{cavity} = -\Omega\sigma_{sintering} = -\Omega\frac{2\gamma_{cavity} - \gamma_{interface}}{R} \tag{2}$$

where Ω is the atomic volume of the (self) diffusing species, $\sigma_{sintering}$ (positive according to Eq. (1)) is the sintering stress, and R is the radius of the spherical cap which relates to the cavity half size of a_{cavity} by $a_{cavity} = R\sin\psi$. Now, as $\Delta\mu_{interface} = 0$, we have $\Delta\mu = \Delta\mu_{cavity} - \Delta\mu_{interface} < 0$, and thus self-diffusion will be directed from the bonded interface to the cavity surface and close the cavity accordingly.

When an arbitrary stress field is applied from faraway, the bonded segment is now stressed, so that the chemical potential change is therefore $\Delta\mu_{interface} = -\Omega\sigma_n$ where σ_n is the applied normal stress. If neglecting the Laplace pressure in Eq. (2), an applied tensile stress will reduce the chemical potential at the bonded interface, thus leading to the self-diffusion from cavity to the interface and to the cavity growth. This is the classic Hull-Rimmer model [31]. Combining the Laplace pressure and the applied stress, we have

$$\Delta\mu = \Delta\mu_{cavity} - \Delta\mu_{interface} = \Omega\left(\sigma_n - \sigma_{sintering}\right). \tag{3}$$

If the applied tensile stress is larger (or lower) than the sintering stress, cavity grows (or shrinks). A more rigorous analysis for the Hull-Rimmer model should consider the chemomechanical equilibrium over the entire interface/surface, as solved by Chuang and Rice [40] and Chuang et al. [41], which will be used later in this section for our bonding fraction evolution equation. In our solid-state-bonding problem, σ_n is negative, so that the diffusion flux is always directed towards the cavity as depicted in Fig. 1(c). This is the diffusive process for cavity closure.

The other process for cavity growth/shrinkage is the creep deformation in Fig. 1(c). No analytical solution can be found in general, except for the Newtonian viscous solid for it is analogous to the elasticity problem when making the replacement of strain rates by strains. Just from a simple dimensional argument, one can see that the magnitude of the volume growth rate will be proportional to the effective creep strain rate in the surrounding material, with its sign governed by the mean stress. But the detailed dependence on the creep stress exponent and stress multiaxiality has to be determined from finite element simulations, as performed extensively by Needleman and Rice [32] and Sham and Needleman [42]. Their solutions can be used to establish curve-fitting equations for our bonding fraction evolution equation, as will be shown shortly below.

In the homogenization model by Tvergaard [27], a square array of cavities with size a_{cavity} and spacing b_{cavity} extends over the entire interface, so that we can define the degree of bonding by

$$f_b = 1 - \frac{a_{cavity}^2}{b_{cavity}^2}. \tag{4}$$

Therefore, our bonding model will be based on the spatiotemporal evolution of the bonding fraction field, $f_b(x_\alpha, t)$, where x_α are the two coordinates spanning the interface.

For the diffusive process, we take a slight modification from the references discussed in the above, given by

$$\frac{df_b}{dt} = -\frac{2\left(1-f_b\right)}{a_{cavity}^3 \ln\left[1/\left(1-f_b\right)\right]}\left(\sigma_n - f_b\sigma_{sintering}\right)\frac{D_B\delta_B\Omega}{k_BT}, \tag{5}$$

where D_B is the interfacial diffusion coefficient, δ_B is the interface boundary thickness of several atomic sizes, k_B is the Boltzmann constant, and T is the absolute temperature. The factor of $1 - f_b$ in the

Table 1
Constitutive parameters used in our CEL simulations of AA6061-T6 [44,45].

A_n (s^{-1})	σ_{ref} (MPa)	n	Q (kJ/mol)
2.41×10^8	22.22	3.55	145

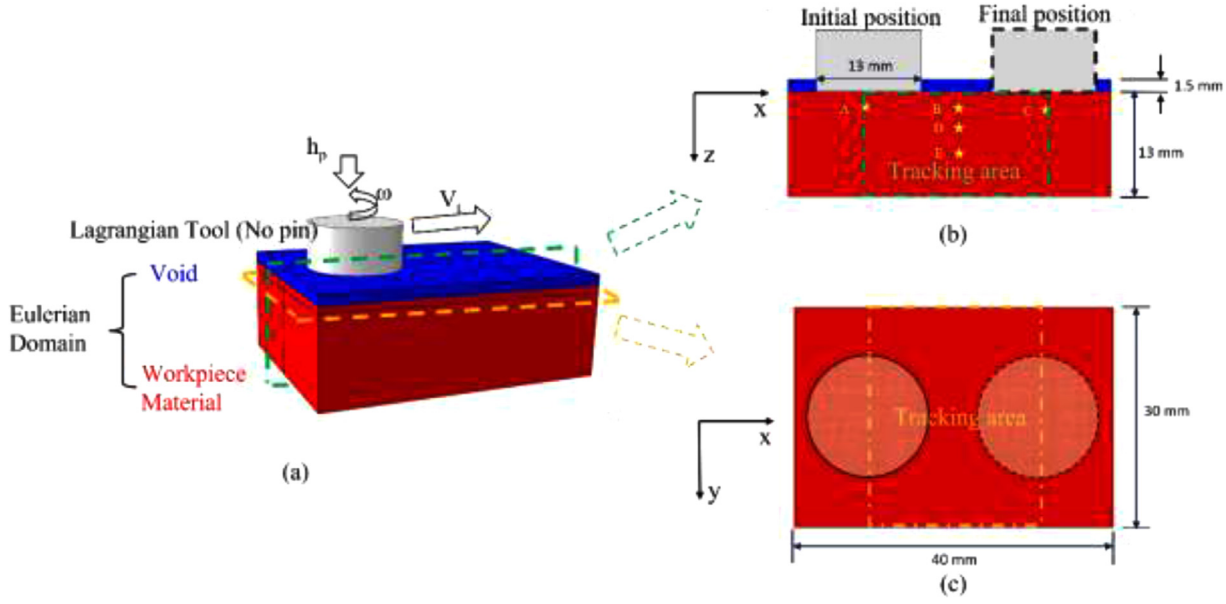

Fig. 3. Finite element setup using the Coupled Eulerian-Lagrangian (CEL) approach for the FSW process. (a) Delineation of various Eulerian and Lagrangian domains in the model. (b) Cross-sectional view of the two workpieces with the dashed box being the tracking area. (c) The cladding-substrate interface with the dashed box being the tracing area.

numerator at the right hand side is introduced merely to regularize the divergence problem at $f_b \to 1$.

For the creep-controlled process, the solution of Sham and Needleman [42] is modified slightly to

$$\frac{1}{f_b}\frac{df_b}{dt} = -(1-f_b)\dot{\varepsilon}^{eff}_{creep} \times \begin{cases} \left[\alpha_n \left|\frac{\sigma_m}{\sigma_e}\right| + \beta_n\right]^n \mathrm{sgn}\left(\frac{\sigma_m}{\sigma_e}\right), & if \left|\frac{\sigma_m}{\sigma_e}\right| > 1 \\ \left[\alpha_n + \beta_n\right]^n \frac{\sigma_m}{\sigma_e}, & if \left|\frac{\sigma_m}{\sigma_e}\right| \le 1 \end{cases} \tag{6}$$

where two dimensionless parameters are introduced for curve fitting to finite element simulations, $\alpha_n = \frac{3}{2n}$ and $\beta_n = \frac{(n-1)(n+0.4319)}{n^2}$, n is the stress exponent in a power-law creep constitutive law, sgn( ) is the sign function, $\dot{\varepsilon}^{eff}_{creep}$ is the effective creep rate (J_2 component, positive definite), σ_m is the mean stress, and σ_e is the Mises stress. Whether the cavity grows or shrinks depends on if $\sigma_m > 0$ or $\sigma_m < 0$. We have added a multiplicative factor of $1/f_b$ to the left hand side of Eq. (6), without which the original Sham-Needleman equation only works when f_b is larger than a critical value (e.g., 0.4).

In realistic FSW conditions, the sintering stress can be neglected as it is usually too low (e.g., a few MPa) as compared to the applied stress. We can now rewrite Eq. (5) in a similar way to Eq. (6), given by

$$\frac{df_b}{dt} = -\frac{2(1-f_b)}{\ln\left[1/(1-f_b)\right]}\dot{\varepsilon}^{eff}_{creep}\left(\frac{\sigma_n}{\sigma_e}\right)\left(\frac{L_{NR}}{a_{cavity}}\right)^3, \tag{7}$$

where L_{NR} is the Needleman-Rice length scale,

$$L_{NR} = \left[\frac{D_B \delta_B \Omega}{k_B T}\cdot\frac{\sigma_e}{\dot{\varepsilon}^{eff}_{creep}}\right]^{1/3}. \tag{8}$$

Neglecting a weak dependence on f_b and stress triaxiality, we have the following

$$\frac{(df_b/dt)_{diffusive}}{(df_b/dt)_{creep}} \propto \left(\frac{L_{NR}}{a_{cavity}}\right)^3, \tag{9}$$

from the comparison between the diffusive and creep-controlled processes. It should be noted that D_B has an Arrhenius dependence on temperature, and so is the creep rate. But their corresponding activation energies are very different, leading to a representative L_{NR} contour plot in Fig. 2(a) for AA6061-T6, with the constitutive parameters given in Table 1 and the diffusion parameters from Frost and Ashby [43]. Overlaid on Fig. 2 are the thermomechanical histories of several representative points on the workpiece-workpiece interface during FSW, as will be discussed later in the next section. Moving towards higher stress and temperature, L_{NR} decreases dramatically, so that the relative significance from diffusive process drops sharply according to Eq. (9). Our preliminary calculations in Wang et al. [33] uses a small a_{cavity} of 1 μm, which already finds little difference between the creep-controlled bonding evolution and the one governed by both processes.

3. Bonding prediction from CEL-based numerical simulations

3.1. Model setup

The coupled-Eulerian-Lagrangian (CEL) finite element simulations were performed to compute the strain rate and temperature fields under the FSW process. As shown by the three-dimensional (3D) CEL model using Abaqus Explicit in Fig. 3, the Eulerian part has a dimension of 40 × 30 × 14.5 mm, including the workpiece domain (thickness of 13 mm) and the "void" domain (thickness of 1.5 mm), with a total of 85,760 EC3D8RT elements. The tool is modeled as a Lagrangian body with a circular bottom of radius a=6.5 mm. Our work here focuses on the relationship between a novel bonding model (Section 2) and the FSW process, so that our initial efforts here adopt an idealized setup, i.e., the tool having no pin or tilt. Certainly, these are important geometric features when comparing our predictions to experimental results. Velocity constraints are applied at model boundaries to avoid material escaping, while the connection between Lagrangian and Eulerian domains is through the Coulomb friction with a fixed friction coefficient of μ_f=0.5 throughout this study.

The workpiece material can be divided into two parts in butt configuration for modeling the FSW process in Fig. 3(b), or into a cladding layer on top of a substrate in Fig. 3(c). The cladding thickness can also be varied systematically, and the example in Fig. 3(c) corresponds to a thickness of 1 mm. All three stages of FSW process were modeled, including plunging of the tool, dwelling, and welding (i.e., laterally moving the tool). The processing parameters are varied in the range of the rotational speed of ω from 600 to 1400 rpm, the welding speed of V_t from

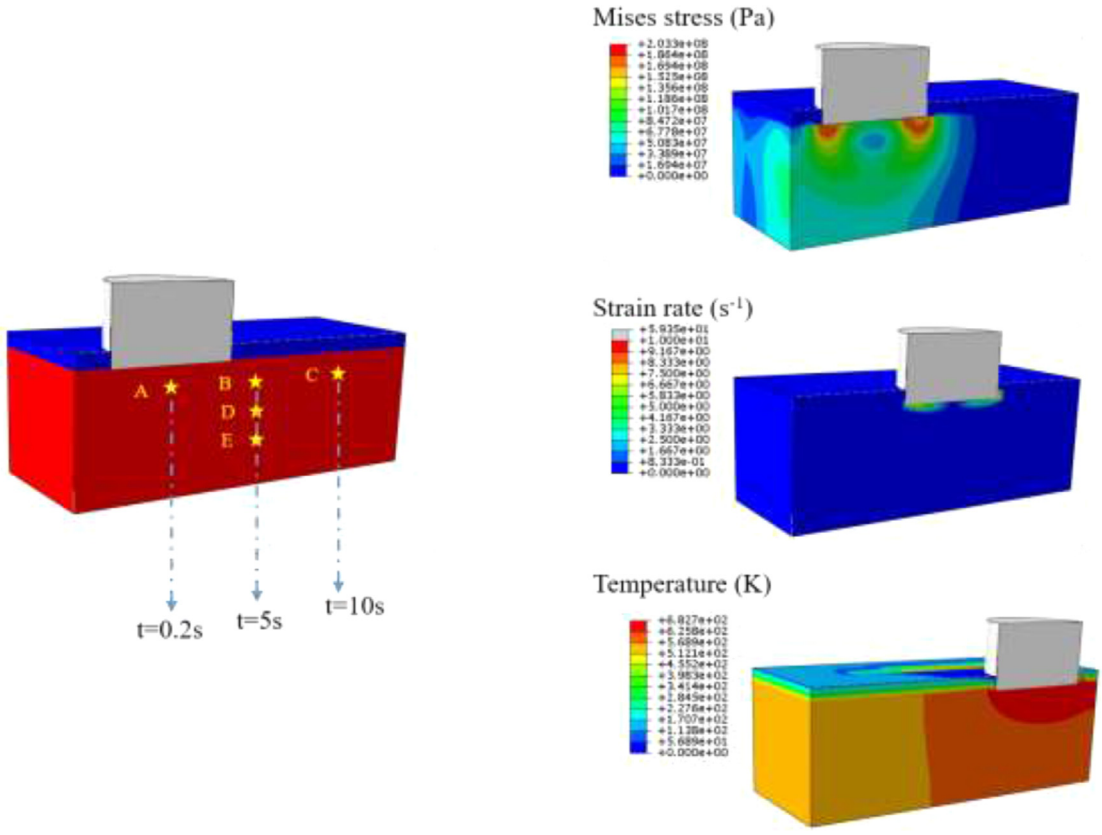

Fig. 4. Representative results from our CEL finite element simulations. Mises stress, strain rate and temperature fields are given, respectively, when the tool center moves right above the locations of A, B and C.

Table 2
Thermomechanical properties for AA6061-T6 [46,47].

Temperature (K)	Specific heat ($Jkg^{-1}K^{-1}$)	Young's modulus (GPa)	Poisson's ratio	Thermal conductivity ($Wm^{-1}K^{-1}$)	Thermal expansion (10^{-6} K^{-1})
298	945	66.94	0.33	162	23.5
373	978	63.21	0.334	177	24.6
422	1000	61.32	0.335	184	25.7
477	1030	56.8	0.336	192	26.6
533	1052	51.15	0.338	201	27.6
589	1080	47.17	0.36	207	28.5
644	1100	43.51	0.4	217	29.6
700	1130	28.77	0.41	229	30.7
755	1276	20.2	0.42	243	-

1 to 3 mm/s, and the plunging depth of h_p from 0.065 to 0.075 mm. The axial force, P, can be calculated afterwards. Additional simulations were also performed without the lateral motion, in order to validate an analytical solution (in Section 4) for the relationship between ω and torque.

The material is modeled by the hyperbolic-sine creep law, given by

$$\dot{\varepsilon}_{creep} = A_n \left[\sinh\left(\frac{\sigma}{\sigma_{ref}}\right)\right]^n \exp\left(-\frac{Q_{creep}}{RT}\right), \tag{10}$$

where A_n is a pre-factor, σ_{ref} is the reference stress, n is the stress exponent, Q_{creep} is the activation energy, and R is the gas constant. The test material of interest is a precipitation-strengthened aluminum alloy, AA6061-T6, with the corresponding parameters given in Table 1 [44,45]. Density of AA6061-T6 is taken as 2690 kg m^{-3}. Other thermomechanical properties used in the simulation are listed in Table 2 [46,47]. The Taylor-Quinney factor that describes the fraction of plastic work to be converted to heat is taken as 0.6.

3.2. Predicted bonding evolution in abutting workpieces

The computed strain rate, stress, and temperature fields from CEL finite element simulations are given by representative examples in Fig. 4. These results are then used as inputs to integrating the bonding evolution equations in Eqs. (5) and (6). The temperature field over the contact zone varies very slowly, but the strain rate and stress fields concentrate near the tool edge and are very sensitive to the interface stick-slip behavior. Therefore, a fine time step (practically found to be less than 1/100 of $2a/V_t$) needs to be adopted when integrating Eqs. (5) and (6) explicitly. Referring back to Fig. 2, we have plotted the stress/temperature histories of points B, D, and E (see their locations in Fig. 3), overlaid with the Needleman-Rice length scale contours in Fig. 2(a) and with the strain-rate contours in Fig. 2(b) in a similar manner to the Ashby deformation map. Before the tool approaches this column of points, the deformation is regular elastoplasticity at room temperature, then followed by rapid heating and thermal softening, and finally reached a steady-state temperature roughly of about 0.7 T_m. The final temperature will not reach or even get close to the melting point; if so, the material will be

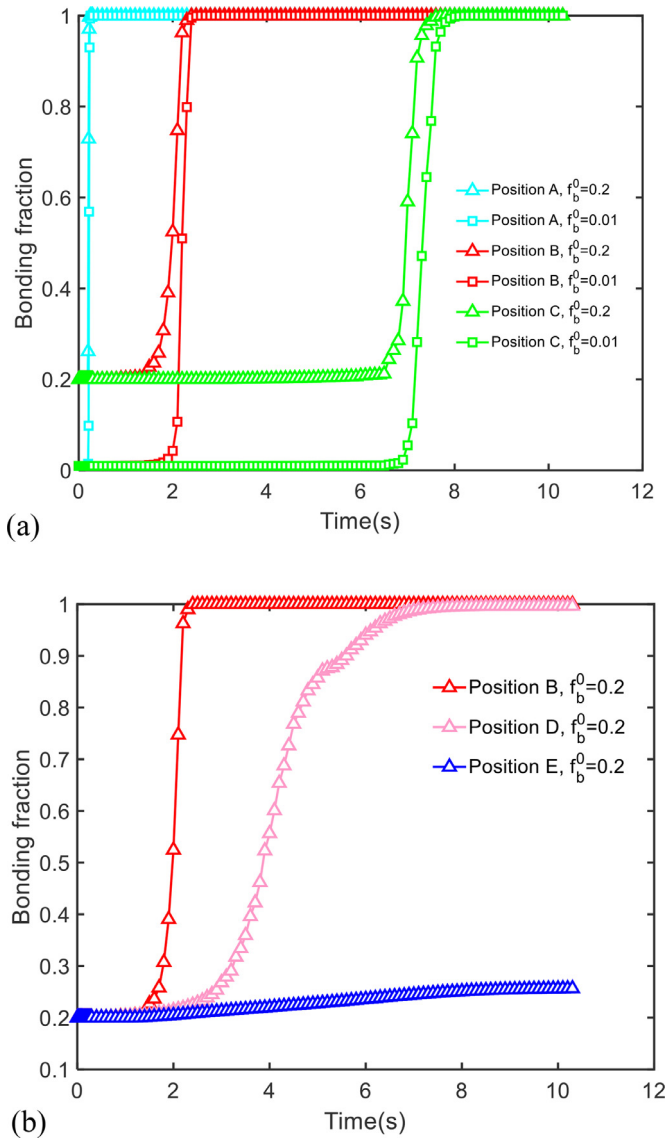

Fig. 5. The evolution of bonding fraction, f_b, for the five reference points in Fig. 3(b), based on the calculated strain-rate and temperature fields from CEL simulations. Two initial values, f_b^0=0.01 and 0.2, represent initially smooth and rough workpiece-workpiece interface.(a) Reference points A, B, and C, moving away in x direction. (b) Reference points B, C, and E, moving away in the depth direction.

extremely soft, and there will be no heating from inelastic deformation due to little resistance to deformation or from frictional heating since the material will be easily moving with the tool. The observed trajectories are therefore universal, as long as thermal softening is incorporated in the constitutive law, e.g., Eq. (10) or the Johnson-Cook law tested before in our work [12].

For the five reference points marked in the rectangular tracking regime on the workpiece-workpiece interface in Fig. 3(b), the evolution of their bonding fractions is presented in Fig. 5, with ω=1000 rpm, h_p=0.07 mm, V_t=2 mm/s, and two initial bonding-fraction values of f_b^0=0.01 and 0.2 (qualitatively representing a rough surface and a well-polished one). As reference points A-C are on the same height but at different x location, their responses are essentially the same except for the corresponding delay in time. As reference points B-E are at different depths, the deepest point E never reaches a meaningful bonding fraction, primarily due to the rapid decay of the strain field with respect to the depth. The final bonding fraction distributions in the tracking area under different rotational speeds are shown in Fig. 6 with the same processing parameters as in Fig. 5 and f_b^0=0.2.

The *first* critical observation from the bonding fraction evolution in Fig. 5 and the final distribution in Fig. 6 lies on the effects of f_b^0. The bonding fraction does not change until the material points enters into the severe thermomechanical process zone. From Fig. 5(a), if a full bonding can be reached, not only the transition from f_b^0 to unity is fast, but also the time for its occurrence is insensitive to f_b^0. From the depth profile in Fig. 6(b), there exists a Heaviside-like behavior of "on" and "off" bonding. Correspondingly in Fig. 6(a), the transition from full bonding (yellow) to no bonding (blue with the initial value f_b^0) is sharp. The location of this on/off interface is insensitive to f_b^0, but a lower value of f_b^0 tends to lead to a long tail that extends far from the on/off interface. As mentioned in Section 2, our model does not have an explicit treatment of surface roughness. Although this appears to be a limitation of our model, various degrees of surface roughness only affects f_b^0, and f_b^0 has negligible effect on the predicted bonding extent. Consequently, these results conclude that the rate-determining process in bonding analysis should be the cavity closure step, but not the rough surface contact analysis (which is otherwise sensitive to f_b^0).

The *second* critical observation from these results pertains to the competition between diffusive and creep-controlled cavity closure processes. All these calculations in Figs. 5 and 6 are based on integrating Eq. (6). Under realistic processing, geometric, and material constitutive parameters used in this FSW analysis, the corresponding results by summing the integrations of Eqs. (5) and (6) have indistinguishable differences from Figs. 5 and 6 when using a_{cavity}>1 μm. Cavities smaller than this size actually fall into the sintering behavior. A mechanistic understanding of such insignificant contribution from diffusive process can be derived from Fig. 2, in which the thermomechanical histories experienced by reference points B, D, and E (different depths) are plotted on top of L_{NR}. The corresponding f_b evolution of these three points is given in Fig. 5(b). Reference point B is the first one to reach the full bonding state, followed by reference point D. On the three trajectories, orange markers indicate when the tool front reaches the x coordinate of these three reference points, and purple markers indicate when the full bonding is reached for B and D and when the tool end leaves E. If a material point experiences a long period of time in high temperature and high strain rate like B and D in Fig. 2(b), it rapidly reaches the full bonding. But reference point E never reaches the full bonding, essentially because the corresponding strain rate field experience by this point is too low. Also the entire thermomechanical trajectory is needed; knowing the start and end points is certainly insufficient as bonding is predicated from integrating Eqs. (5) and (6). For the successful bonding in referent points B and D, the corresponding L_{NR} is extremely low. As the relative significance of diffusive and creep-controlled cavity closure processes is dictated by $(L_{NR}/a_{cavity})^3$ in Eq. (9), it now becomes obvious that diffusive process has almost no contribution to the chosen FSW processing parameters. In other words, "diffusion bonding" as suggested by almost all solid-state-bonding studies is actually creep-controlled, but not governed by diffusive process.

For the sake of practical consideration and also noting the mesh size limitation, the critical value for the full bonding to take place is adopted as 0.8, as shown by the example in Fig. 6(b). From results in Fig. 6(c) and Fig. 7, it is found that the bonding extent in the depth direction increases with the increase of tool rotational speed ω (mainly because of the corresponding increase of the strain-rate level), with the decrease of tool traveling speed V_t (for a longer time in the severe thermomechanical process zone), and with the increase of plunging depth h_p (due to the increased stress level). These trends agree qualitatively with the experimental discussions in the introduction section. A question that naturally arises is the maximum bonding depth, as these predicted values are still less than half of the tool radius (6.5 mm here). The answer will be addressed from our analytical solution in Section 4.

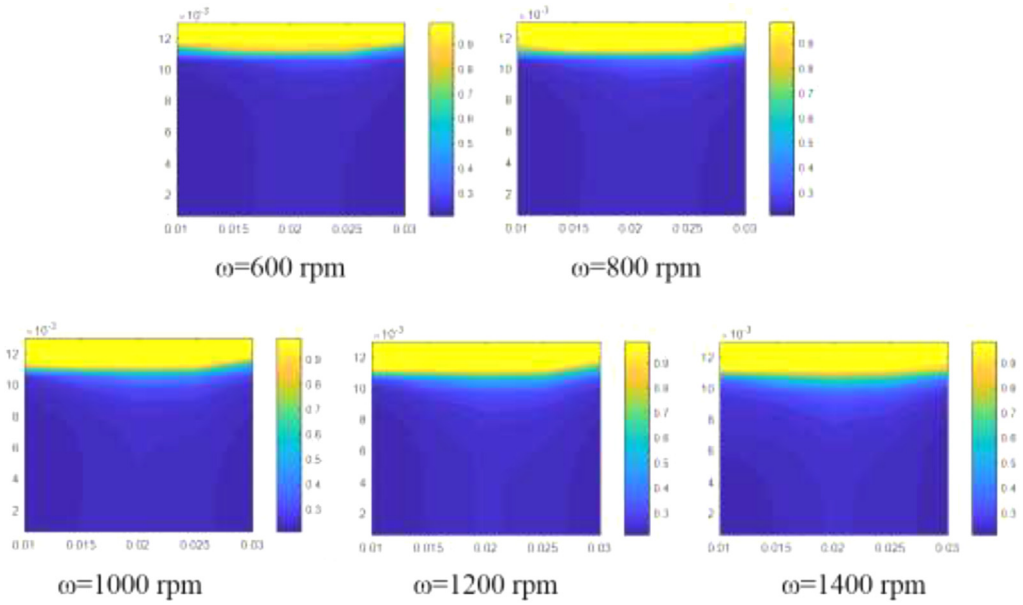

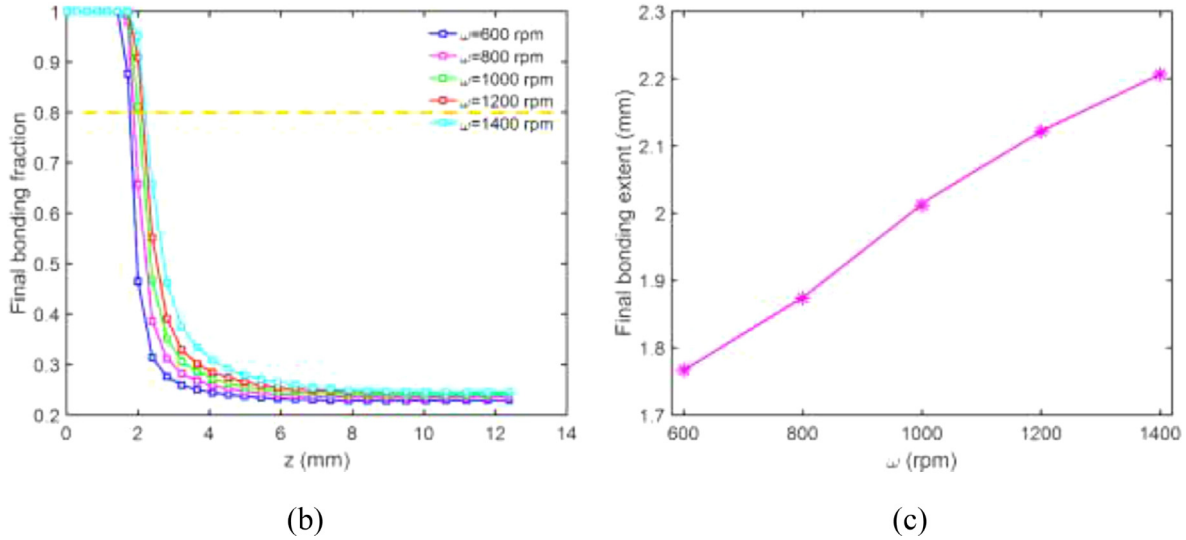

Fig. 6. (a) Contour plots of the final bonding fraction with respect to varying ω for the FSW process in Fig. 3(b), with V_t=2 mm/s and h_p=0.07 mm. (b) The corresponding bonding fraction distribution in the depth direction. (c) The bonding extent with respect to varying ω when taking the critical bonding fraction for full bonding as 0.8.

3.3. Predicted bonding evolution in cladding configuration

A variant form of FSW that also finds widespread applications is the bonding for the cladding-substrate configuration in Fig. 3(c). The calculation procedure is the same as the above subsection, with the results given in Figs. 8 and 9 for a cladding thickness of d=1 mm. Results in Fig. 8(a) correspond to the instant when the tool center arrives the right boundary of the rectangular tracking zone in Fig. 3(c), so that the adjacent area has not reached the full bonding because of insufficient time in the high strain-rate state. The bonding distribution along the y direction again shows a Heaviside-type transition with long tails extending to faraway whereas the sensitivity to f_b^0 is found. With the increase of ω or h_p, or with the decrease of V_t, the bonding extent in lateral direction increases, but all these results are close to the tool radius of 6.5 mm for the range of processing parameters used in these studies. Increasing the cladding thickness will reduce the bonding extent dramatically, which will be elaborated later in Section 5.

4. An analytical model for the prediction of bonding extent in FSW

Based on the Hill-Bower similarity analysis [48–50], we notice that, for a pure-creeping solid, the instantaneous deformation field is the same as a nonlinear elastic contact problem if the correspondence between strain rates in the former and strains in the latter is made. Furthermore, based on the solution analogy between Newtonian viscous material and Hookean solid, we have developed an approximate yet analytical solution to relate the resulting torque and total heat generation rate to the stick-slip ratio of c/a [12]. In the next, we will give a concise review of the contact solutions, and then extend this line of analysis to derive an

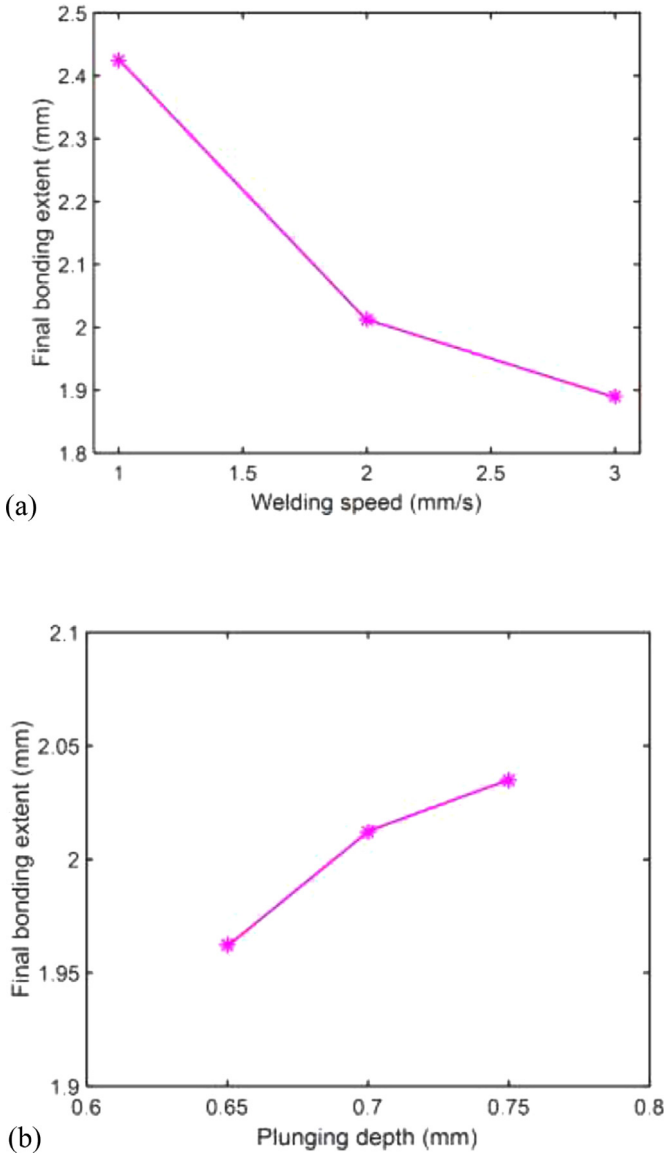

Fig. 7. The final bonding extent for the FSW process in Fig. 3(b). (a) Varying V_t with ω=1000 rpm and h_p=0.07 mm. (b) Varying h_p with ω=1000 rpm and V_t=2 mm/s.

approximate yet analytical solution to relate the final bonding extent to the processing parameters (such as the axial load and the tool rotational speed).

As shown in Fig. 10, the interface shear stress is limited by the Coulomb friction stress,

$$\tau'_{\theta z} = \frac{\mu_f P}{2\pi a^2}\frac{1}{\sqrt{1-(r/a)^2}}, \tag{11}$$

where μ_f is the friction coefficient. For infinite friction ($\mu_f = \infty$), the shear stress distribution that generates a rotational displacement field of the form of $u_\theta = r\theta$ (i.e., exactly following the spinning rigid indenter) is given by

$$\tau_{\theta z}\big|_{\mu=\infty} = \frac{3M^*}{4\pi a^3}\frac{r/a}{\sqrt{1-(r/a)^2}}, \tag{12}$$

where the torque parameter M^* remains to be determined. Under finite friction, the shear stress distribution can be taken as the lower one of the above two solutions, as shown by the dashed red curve in Fig. 10. Equating these two solutions at $r = c$ determines the value of M^*. Therefore, the shear stress solution is approximately,

$$\tau_{\theta z}\big|_{\mu<\infty} = \frac{\mu_f P}{2\pi a^2}\begin{cases}\frac{a}{c}\frac{r/a}{\sqrt{1-(r/a)^2}}, & r \le c: \text{ stick}\\ \frac{1}{\sqrt{1-(r/a)^2}}, & c \le r \le a: \text{ slip}\end{cases} \tag{13}$$

The resulting torque on the tool, as given by $M_z = \int_0^a \tau_{\theta z}|_{\mu<\infty} 2\pi r dr$, can be written in a dimensionless function,

$$\frac{2}{3}\Big|_{c/a=1} \le \frac{M_z}{\mu P a} = \Pi_M(c/a) \le 0.78|_{c/a=0}. \tag{14}$$

Now because the main processing parameters are ω, h_p, and V_t, we need to find the dependence of the normalized torque, $M_z/\mu Pa$, on ω (which certainly needs an appropriate way to normalize). As $V_t << \omega a$, we conduct additional numerical simulations in Fig. 3 with the removal of the lateral moving of the tool. The resulting relationship of $M_z/\mu Pa \sim \omega$ is given in Fig. 11, showing a reduction of torque with the increase of tool rotational speed, but the ordinate range falls within predictions in Eq. (14).

The elastic twisting contact solution for infinite friction is of the form in Eq. (12), leading to the following relationship between the rotation angle Θ and the torque [51]:

$$\Theta|_{\mu_f=\infty} = \frac{3M_z}{16Ga^3}, \tag{15}$$

where G is the shear modulus. This solution works for $\mu_f = \infty$ and thus $c/a \to 1$. In general, we need to multiply Eq. (15) by a dimensionless function $\Phi(c/a)$,

$$\Theta|_{\mu_f<\infty} = \frac{3M_z}{16Ga^3}\Phi(c/a). \tag{16}$$

The friction coefficient does not explicitly enter into this dimensionless function due to the dependence of c/a on μ_f. From the solution analogy between Newtonian viscous material and Hookean solid, strains in elastic solution will be replaced by strain rates, and shear modulus by viscosity, so that the corresponding solution for our problem is

$$\omega = \frac{3M_z}{16\eta a^3}\Phi(c/a). \tag{17}$$

where the shear viscosity can be evaluated from the material constitutive law in Eq. (10).

Results from CEL simulations are given in Fig. 12 for five different values of ω. In the elastic solution of Eq. (16), when $c/a \to 0$, the rotation angle approaches infinity. Therefore, from the two limits: $\Phi(c/a = 1) = 1$ and $\Phi(c/a \to 0) \to \infty$, Fig. 12 can be fitted to a tangent function of the form of

$$\Phi\left(\frac{c}{a}\right) = 6.98\tan\left[\frac{\pi}{2}\left(1-\frac{c}{a}\right)\right] + 1. \tag{18}$$

Substituting Eq. (18) into Eq. (17), we now make a connection between c/a and ω.

In Section 3, we have already shown that the diffusive process in Eq. (5) contributes insignificantly as compared to the creep-controlled process in Eq. (6). As the mean stress is negative in our FSW process, we rewrite Eq. (6) into a simplified form,

$$\frac{df_b}{dt} = f_b(1-f_b)\dot{\varepsilon}^{eff}_{creep}C_0\left(n, \left|\frac{\sigma_m}{\sigma_e}\right|\right), \tag{19}$$

with C_0 being a dimensionless function. Rearranging and integrating this equation gives

$$\int_{f_b^0}^{f_b^{final}} \frac{1}{f_b(1-f_b)} df_b = \int_{t=0}^{t=t^*} C_0\dot{\varepsilon}^{eff}_{creep} dt. \tag{20}$$

As shown by the strain rate and temperature fields in Fig. 4, the right-hand-side integrant is only large when the material point enters below the tool (or into the thermomechanical process zone). Thus the

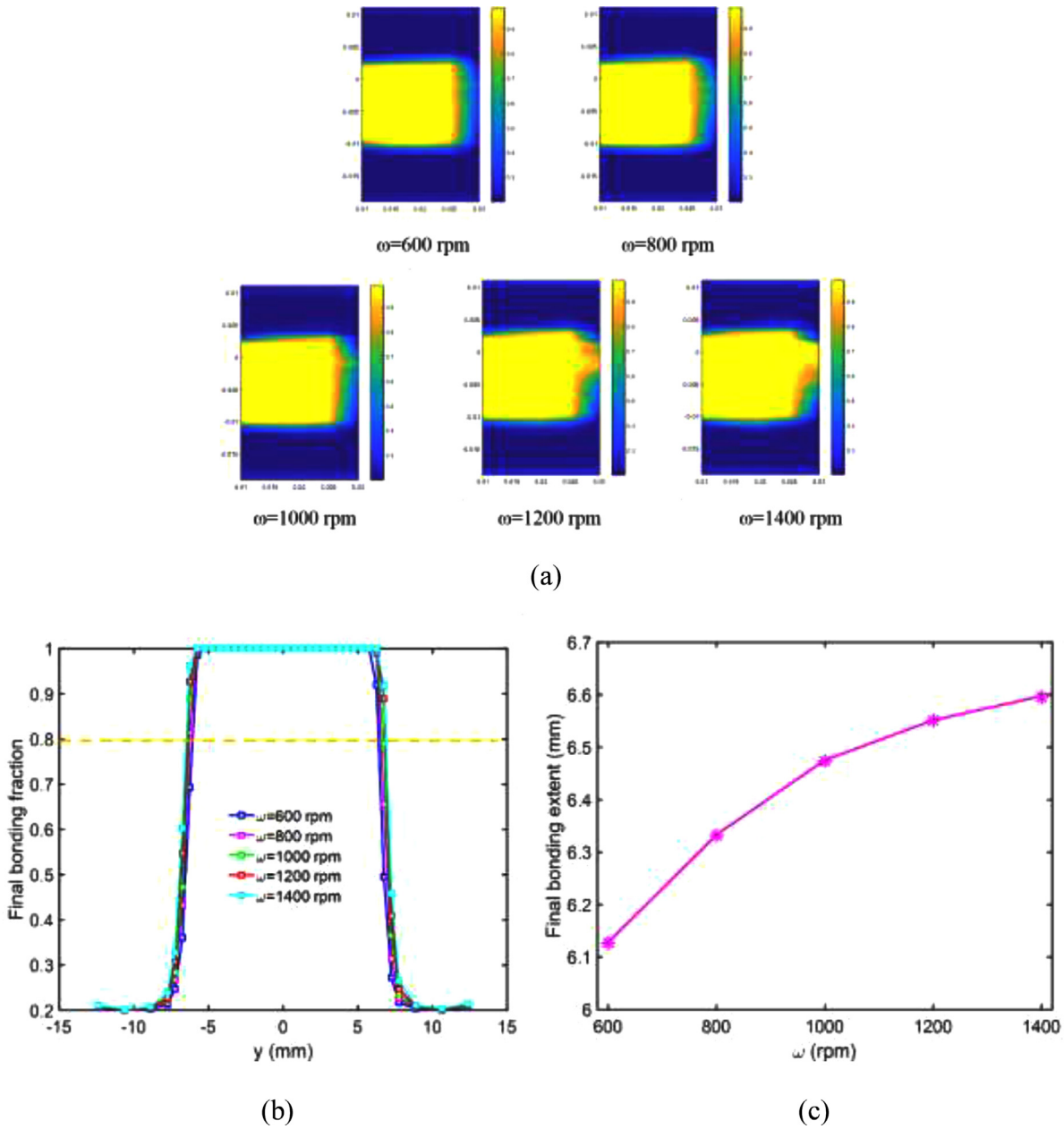

Fig. 8. (a) Contour plots of the final bonding fraction with respect to varying ω for the cladding problem in Fig. 3(c), with V_t=2 mm/s and h_p=0.07 mm. (b) The corresponding bonding fraction distribution along the dashed line in Fig. 3(c). (c) The bonding extent with respect to varying ω when taking the critical bonding fraction for full bonding as 0.8. In these calculations, the cladding thickness is d=1 mm.

elapsed time can be approximated by $2a/V_t$, and $\dot{\varepsilon}^{eff}_{creep}(x_i,t)$ can take the highest value, $\dot{\varepsilon}^{eff}_{creep,\max}(x_i)$, over this entire elapsed time, leading to

$$\left[\ln\left(\frac{f_b}{1-f_b}\right)\right]_{f_b^0}^{f_b^{final}} \approx C_0\dot{\varepsilon}^{eff}_{creep,\max}\frac{2a}{V_t}. \tag{21}$$

For the FSW process, one primary interest is the prediction of bonding depth. For the steady state problem in Fig. 13(a), we only need to find $\dot{\varepsilon}^{eff}_{creep,\max}(z)$. Contact problems have an inverse square root decay of the deformation fields, so that we introduce the following

$$\dot{\varepsilon}^{eff}_{creep,\max} \approx \frac{\omega}{\left(\frac{z}{c}\right)^2 E\left(\frac{c}{a}\right)}, \tag{22}$$

where the dimensionless function $E(c/a)$ is introduced to consider the dependence on interface stick-slip condition (which does not permit analytical solution, thus requiring curve fitting for this dimensionless function). Combining all the above equations, we now have the final bonding fraction at a given depth of z by

$$\ln\left[\frac{f_b^{final}(z)}{1-f_b^{final}(z)}\right] \approx \ln\left(\frac{f_b^0}{1-f_b^0}\right) + C_0\frac{\omega}{(z/c)^2E(c/a)}\frac{2a}{V_t}. \tag{23}$$

Similarly, for the FSW cladding problem in Fig. 13(b), the bonding extent in the lateral direction is derived as

$$\ln\left[\frac{f_b^{final}(y)}{1-f_b^{final}(y)}\right] \approx \ln\left(\frac{f_b^0}{1-f_b^0}\right) + C_0\frac{\omega}{\frac{y^2+d^2}{c^2}E\left(\frac{c}{a},\frac{d}{a}\right)}\frac{2a}{V_t}, \tag{24}$$

in which the dimensionless function $E(c/a, d/a)$ again needs to be curve fitted by comparing this equation to the bonding fraction calculations based on the actual strain-rate and temperature fields in CEL numerical simulations.

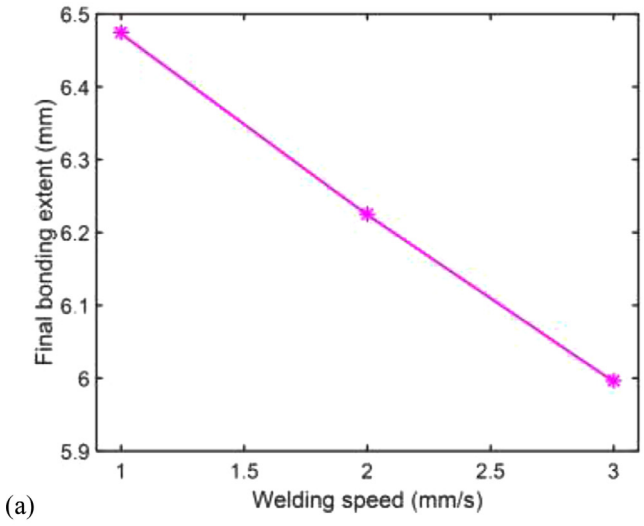

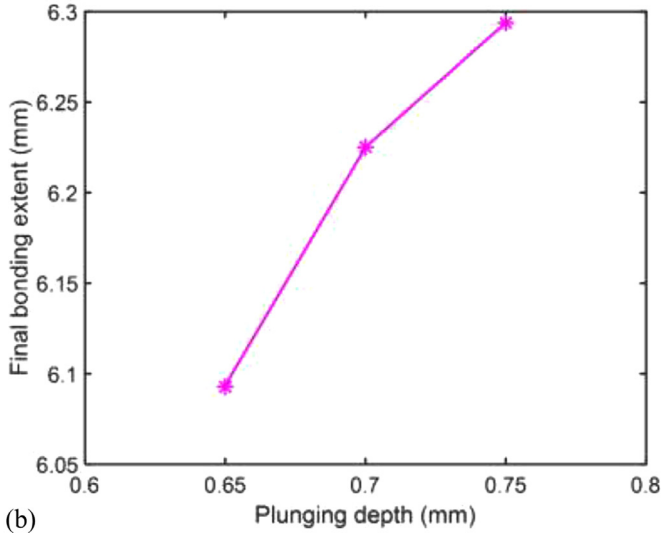

Fig. 9. The final bonding extent for the FSW cladding process in Fig. 3(c). (a) Varying V_t with ω=1000 rpm and h_p=0.07 mm. (b) Varying h_p with ω=1000 rpm and V_t=2 mm/s.

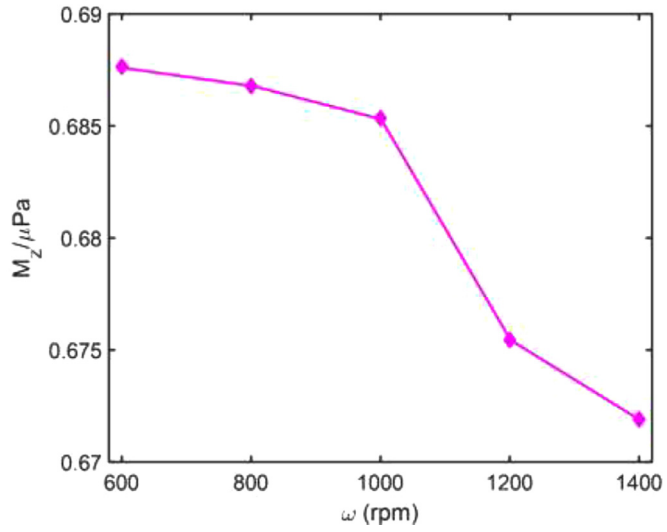

Fig. 11. From CEL finite element simulations Fig. 3 (but with the lateral motion turned off), the normalized torque, $M_z/\mu_f Pa$, is plotted against the tool rotational speed, ω.

The key steps for the bonding fraction prediction are now summarized into the flowchart in Fig. 14, as discussed below.

(1) Given all the processing parameters (ω, V_t, and h_p or P), material constitutive parameters in Eq. (10), and geometric parameters (a and tool shape). The most important ones are ω and P, as they are easily and practically accessible in the FSW technique.
(2) As the stick-slip ratio is not known a priori, an iterative procedure in the shaded box is needed.
   a At the beginning of the $(K+1)$-th iteration, we know $(c/a)|^K$.
   b Determine the normalized torque from $\frac{M_z}{\mu Pa} = \Pi_M(c/a)$, and the total heat generation rate from $Q_{total} = \omega M_z$ (true only when the Taylor-Quinney factor is α_{TQ}=1).
   c Numerical simulations in Fig. 4 exhibit a large thermally affected zone, so that the temperature near the tool can be calculated from $T_{\max} = T_0 + \frac{Q_{total}}{2\pi ka}$, where k is the thermal conductivity, based on the Rosenthal solution for a circular zone of heat source on a half space [52].
   d Based on the mean contact pressure (because P is given) and the above temperature, we determine the corresponding material viscosity from the material constitutive law in Eq. (10).

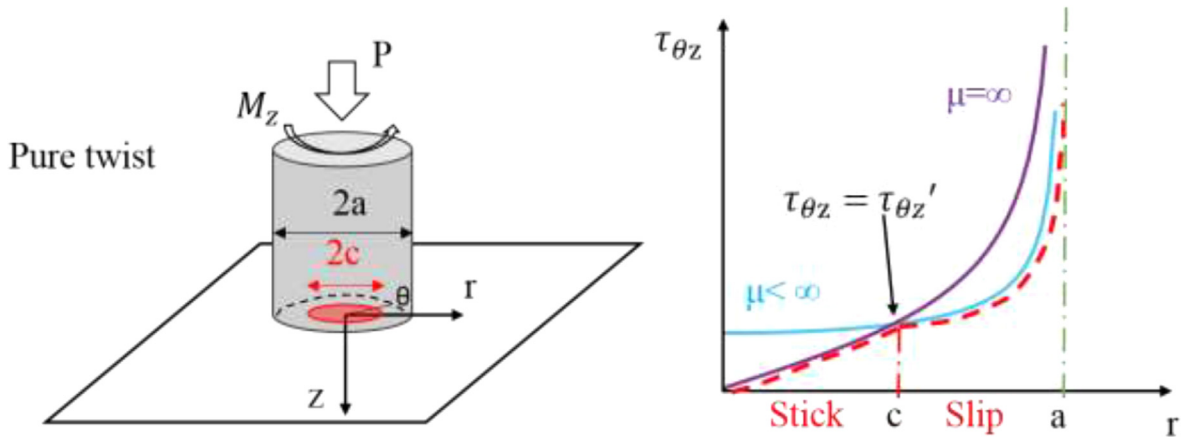

Fig. 10. Our analytical model of the interface stick-slip behavior and the shear stress distribution. There exists an annular sliding zone ($c \le r \le a$) in which the theoretical shear stress at infinite friction is larger than the Coulomb friction as determined from the normal pressure distribution. The red dashed curve represents our approximate yet analytical solution. The resulting strain rate field in the substrate provides the critical input for bonding analysis.

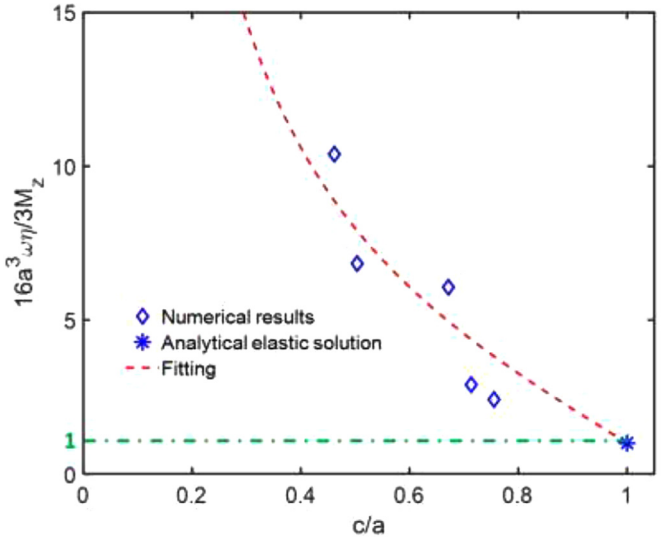

Fig. 12. A dimensionless parametric group, combining ω, a, M_z, and workpiece material viscosity of η, is plotted against the stick-slip ratio of c/a. Blue diamonds are CEL simulation results with five different values of ω. Blue asterisk is the analytical solution at c/a=1. The red dashed curve represents a fitting equation, to be used to construct our flowchart in Fig. 14.

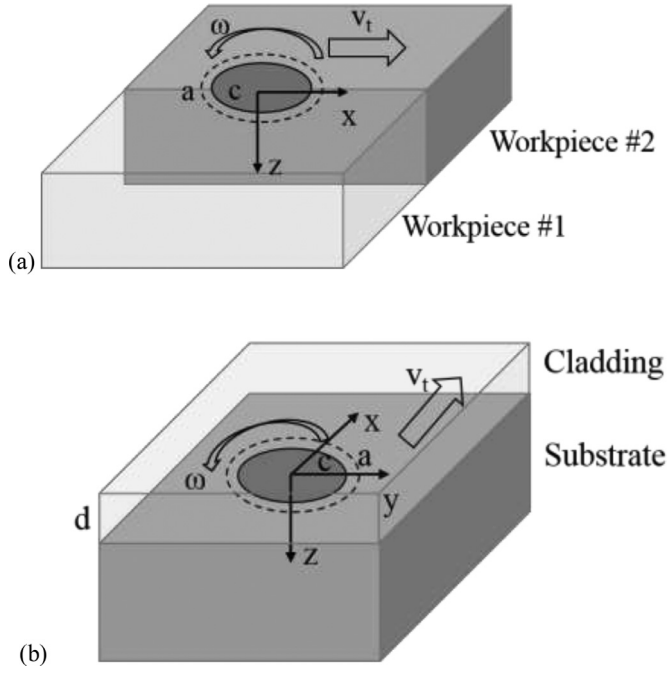

Fig. 13. Schematic illustrations of the coordinates, stick-slip behavior, and interfaces in our bonding analysis, in which (a) corresponds to Fig. 3(b), and (b) corresponds to Fig. 3(c).

e Using the normalized function $\Phi(c/a)$ in Eqs. (17) and (18) to obtain a new stick-slip ratio of $(c/a)|^{K+1}$.

f Check the convergence of $|(c/a)^{K+1} - (c/a)^K|$ and determine if next iteration is needed.

(3) Upon the determination of c/a, we can use Eq. (23) or Eq. (24) to calculate the final bonding fraction of a given material point. The fitting equation for $E(c/a)$ will be given later in Fig. 16.

It should be pointed out that the fitting equations presented in this Section are primarily functions of the interface stick-slip parameter, c/a, but are insensitive to material constitutive parameters and others, essentially because of the universality of the similarity contact analysis and the Newtonian-Hookean analogy. Admittedly, E functions in Eqs. (22) and (24) will depend on tool pin and other geometric features which can nevertheless be easily incorporated.

5. Comparisons between numerical and analytical models

This section aims to validate the bonding extent prediction from comparing the analytical solution (using the flowchart in Fig. 14) to the detailed calculations in Section 3 (using the CEL-simulated fields as inputs to the bonding fraction evolution equations in Section 2).

For the FSW process in Fig. 3(b) and the results in Figs. 5-7, plotted in Fig. 15 are the final bonding fraction distributions in the depth direction with a wide range of ω values. The numerical results are the same as in Fig. 6(b). As explained in the previous section, the strain rate fields have a dependence on c/a that does not permit analytical solution. To this end, for each of these five ω values, we can read their corresponding c/a values from CEL simulations, adjust the E value in Eq. (23) to find agreements between the solid and dashed curves in Fig. 15, and thus obtain a relationship between E and c/a, as presented in Fig. 16. Also noting the form of $\Phi(c/a)$, we can curve the discrete diamond markers in Fig. 16 by

$$E\left(\frac{c}{a}\right) = -2250\tan\left[\frac{\pi}{2}\left(1-\frac{c}{a}\right)\right] + 3070. \tag{25}$$

This fitting equation completes the flowchart in Fig. 14.

For the FSW cladding process in Fig. 3(c) and the results in Figs. 8 and 9, plotted in Fig. 17 are the final bonding fraction along the lateral direction for different cladding thickness values. In Eq. (24), the particular form of $(y^2+d^2)/c^2$ is assumed because of the inverse square decay of the deformation fields upon contact. In spite of tuning the dimensionless function of $E(c/a, d/a)$, predictions from our flowchart in Fig. 14 show the same trends as the numerical results, especially for the thickness dependence. We choose a total of six different thickness values, and keep other processing parameters as ω=1000 rpm, V_t=2 mm/s, and h_p=0.07 mm. It can be seen that there is a sudden "on/off" transition when d increases from 2 to 3 mm, exactly in the same manner as the z-axis distributions of bonding fraction in Figs. 6 and 7. Consequently, we can directly use the bonding extent in the FSW process as the critical cladding thickness in the FSW cladding process.

Upon the fitting and validation of our analytical solution and the flowchart in Fig. 14, we now aim to construct a bonding map with respect to the processing parameters. That is, with varying ω and P like in the actual applications, what is the corresponding bonding extent in FSW? Do we also see a sudden "on/off" transition between full bonding and no bonding? Can a process window be determined with respect to these input parameters? Answers to these questions are given in Figs. 18 and 19. In our CEL simulations, the tool plunging depth is prescribed, but the axial pressure can be calculated as a result. The predicted c/a and bonding extent for the FSW process with respect to ω and P is given in Figs. 18 and 19, respectively, where surfaces are from our flowchart in Fig. 14 and discrete triangles correspond to five different ω values from CEL simulations in Fig. 3(b). The collapse of discrete triangles onto the surfaces validates the success of our analytical solution and flowchart analysis. These 3D plots resemble cliffs on a terrain map, indicating the sharp "on/off" transition as exactly have been seen in Figs. 6 and 8. With the increase of ω and P, the bonding extent sees a rapid jump from zero to almost half of the tool radius. This upper bound is essentially due to the rapid decay of strain rate fields in the depth direction.

The bonding map in Fig. 19 can be used to find the process window for the design and improvement of FSW processes. As a rule of thumb, the bonding extent sees a binary "on/off" transition, and the maximum bonding extent lies within the thermomechanical process zone, or simply half of the tool radius. Further validation of this bonding map requires additional FSW experiments as most of them in literature do not have direct bonding measurements.

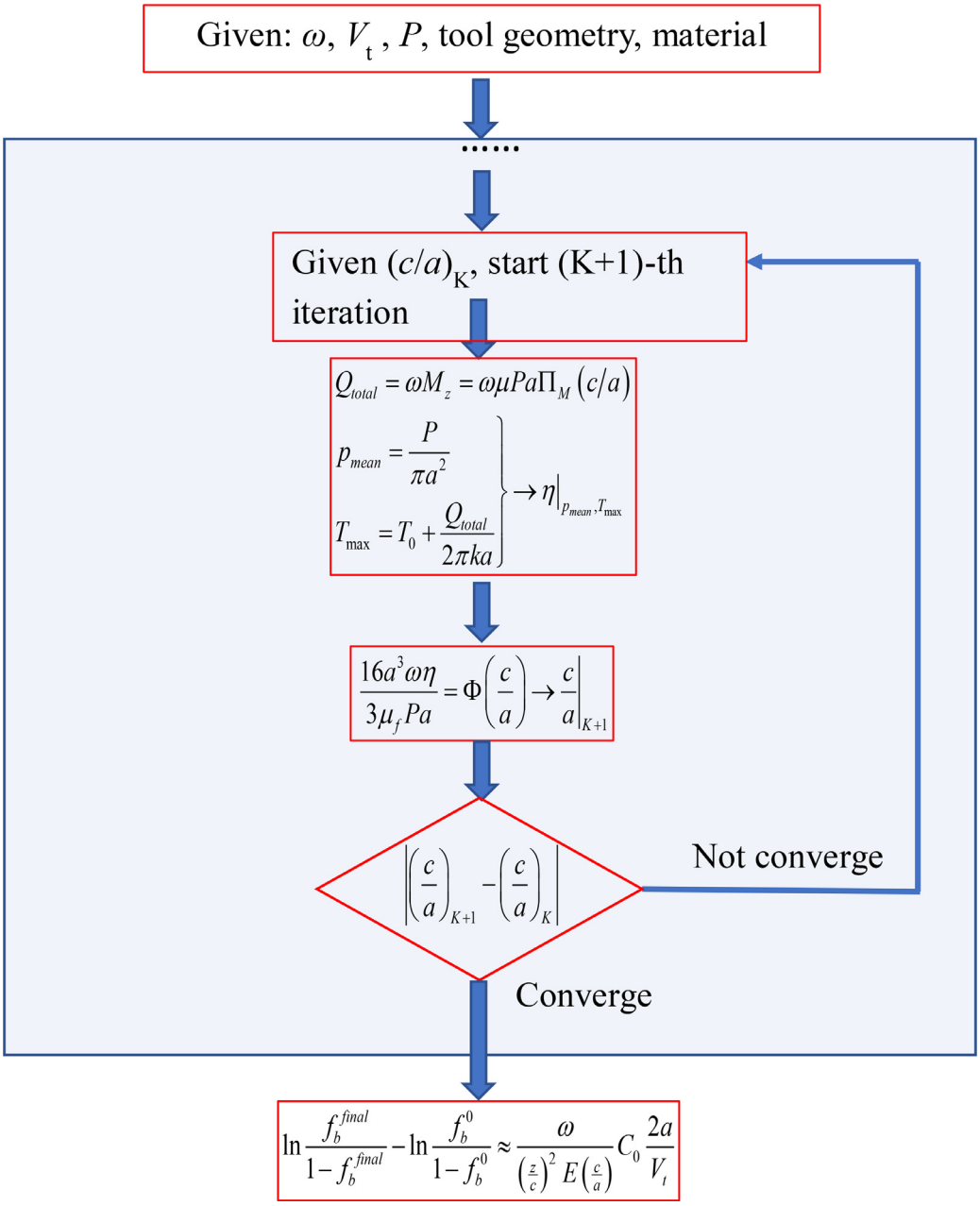

Fig. 14. A flowchart representing our approximate yet analytical solution from the processing, geometric, and material constitutive parameters to the bonding fraction evolution.

6. Further comparisons to experiments

The FSW community has been fully aware of the shallow bonding depth, regardless of the energy input. As reviewed extensively in [8,9], the use of pins on the tool bottom, together with their complex shapes and patterns, aims partially to extend the deformation fields in the depth direction. For the first time, a mechanistic bonding model is proposed here that relates the bonding evolution to the thermomechanical fields, particularly strain rate and temperature, through Eqs. (5) and (6) that are general for any type of solid-state bonding techniques. Specifically, for the FSW process, based on our stick-slip contact analysis, we can derive an analytical expression of such thermomechanical fields in Section 4, so that the dependence of bonding extent on processing parameters can be predicted and validated by our simulated thermomechanical fields. The resulting figure or merit in Fig. 19 can be qualitatively justified by nearly all FSW experiments, i.e., the need to increase rotation speed and axial force for an extended bonding in depth direction.

While a quantitative comparison between our prediction in Fig. 19 and experiments awaits further investigation, a few observations and some literature works suggest the validity of such predictions. First, although experimentally it is known that the bonding extent does not go far than the shoulder radius or pin length, this has not been theoretically explained until the model development here, e.g., Eqs. (21)–(24). The key reason lies on the rapid decay of the strain rate field from the contact problem, which exacerbates further if a small stick-slip ratio is developed. Our model presented in this work presents an upper bound prediction. Second, there are a few indirect studies that support the sharp rise in Fig. 19. For example, Panda et al. [53] applied the FSW process onto the top surface of two stacked plates. The top layer was thin enough for the plate-plate interface to be bonded, and the bonding quality of the two plates was tested in a two-dimensional lap-shear con-

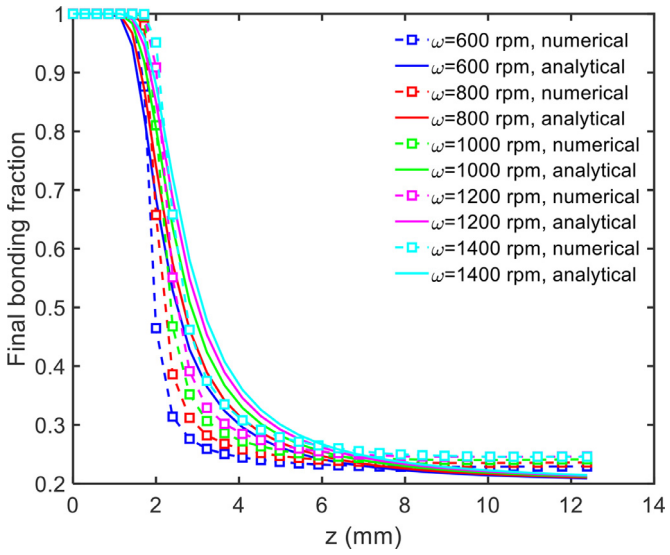

Fig. 15. Comparisons between the CEL numerical simulation results in Fig. 6(b) and our analytical model for the bonding fraction distribution along the depth direction in the FSW setup in Fig. 3(b).

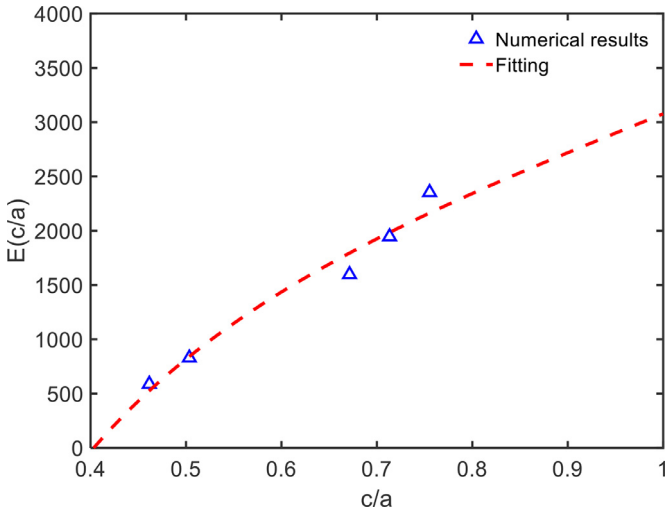

Fig. 16. The dimensionless function, $E(c/a)$, in the flowchart of Fig. 14.

figuration. These authors found a dependence of the pull-off force for fracture on the tool axial force and rotation speed in a similar manner as the sharp rise features in Fig. 19. Noting that their failure modes are nearly all shear failure, the failure force can be estimated by the product of the shear strength and the bond width. Apparently, their findings on failure force agree qualitatively with our predictions in Fig. 19. Third, there are further evidences from the friction stir spot welding (FSSW) process [54]. According to predictions in Fig. 17, if the horizontal interface moves farther from the contact surface, the bonding width shrinks significantly when the processing parameters remain unchanged. Similarly, given a fixed depth, the bonding width will evolve with respect to tool rotation speed and axial force (that is, the energy input) in the same manner as in Fig. 19. That is, we will see a sharp rise of the bonding width, but the plateau will never exceed the tool radius/diameter. Preliminary results in [54] also show the detailed information of cavities and their distributions. A close comparison of these experiments to our modeling effort here will be presented in a future study.

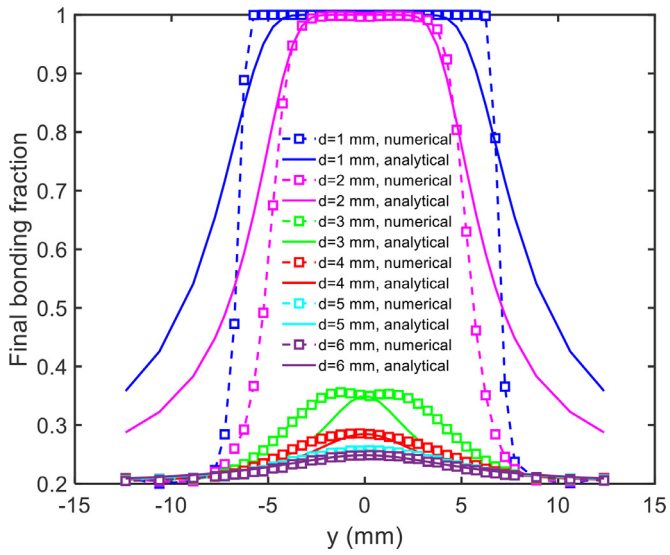

Fig. 17. The final bonding fraction distribution on the cladding-substrate interface along the dashed line in Fig. 3(c), with respect to various choice of cladding thickness of d.

7. Summary

A mechanistic understanding of bonding behavior under various operation conditions of the FSW process is critical in its successful engineering applications. There are three main contributions in this work as shown below.

(1) *Bonding Model*: Most solid-state-bonding models rely on rough surface contact and volumetric inter-diffusion for interfacial gap closure. Here we propose a completely different viewpoint, based on the well-established knowledge in grain boundary creep fracture of high temperature polycrystalline materials. The interfacial cavities will shrink under the combined action of sintering and applied compressive stresses via the Hull-Rimmer diffusive process, or under the creep-controlled deformation process. The competition between these two processes is dictated by the Needleman-Rice length scale, L_{NR}. When plotting the thermomechanical histories of materials under FSW tool, one can thus immediately tell that diffusive process plays a negligible role in the bonding evolution. Thus, the solid state bonding under FSW relies mainly on the creep strain rate in the adjourning workpieces, weakly on stress triaxiality, and negligibly on interfacial diffusion.

(2) *Predicting bonding evolution from CEL simulation results*: Using the calculated strain rate and temperature fields from CEL finite element simulations, we can predict the evolution of the bonding fraction. These results are insensitive to the initial bonding fraction, suggesting that a rough surface contact analysis be not needed. The bonding extent increases with the increase of tool rotational speed and plunging depth, or with the decrease of tool welding speed. The maximum bonding extent in the FSW process, as well as the maximum cladding thickness that can be made full-bonded in the FSW cladding process, is found to be about half of the tool radius.

(3) *Bonding Map and Process Window*: Based on the Hill-Bower similarity analysis and the solution analogy between Newtonian viscous material and Hookean solid, we can derive an approximate yet analytical solution to predict the bonding extent. The resulting bonding map shows that the dependence of bonding extent on processing parameters (mainly ω and P) shows a sharp transition between no bonding and full bonding. The analytical prediction agrees well with numerical simulations, thus providing a process window for future design and applications of this FSW technique.

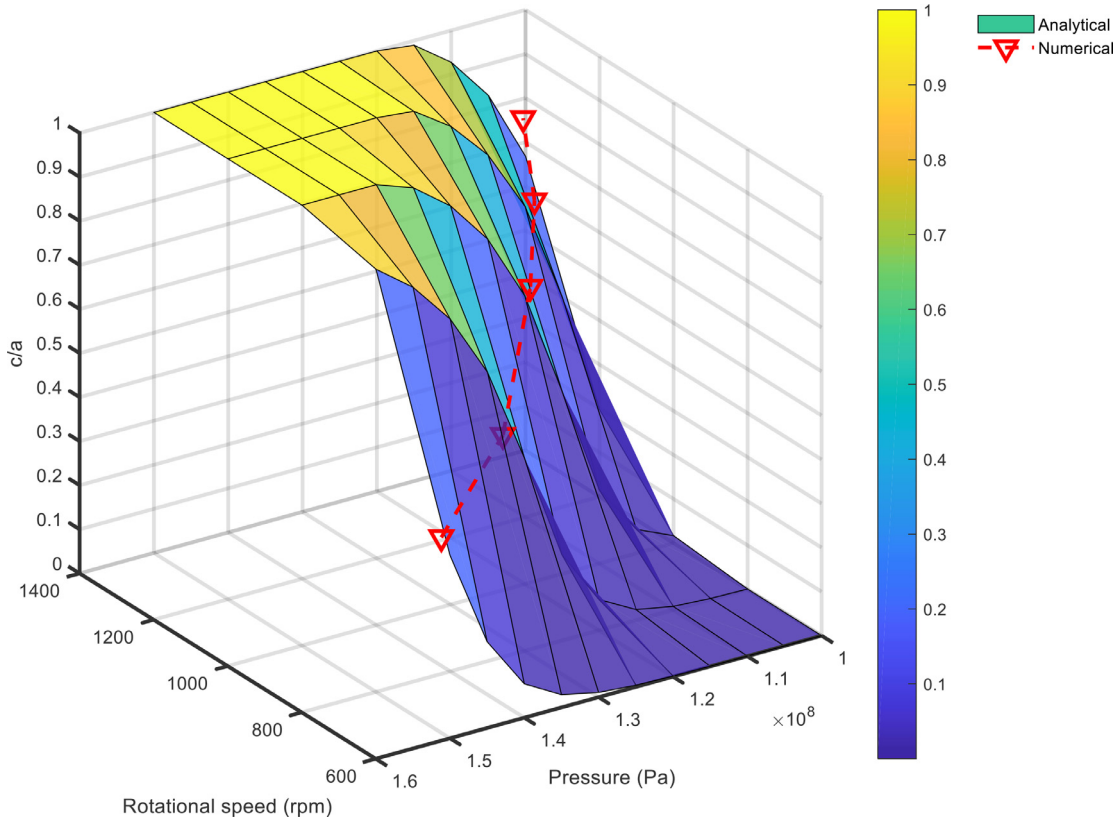

Fig. 18. The stick-slip ratio with respect to two processing parameters (axial pressure and tool rotational speed), obtained from the CEL numerical simulations of the FSW setup in Fig. 3(b) and our analytical solution based on Fig. 14.

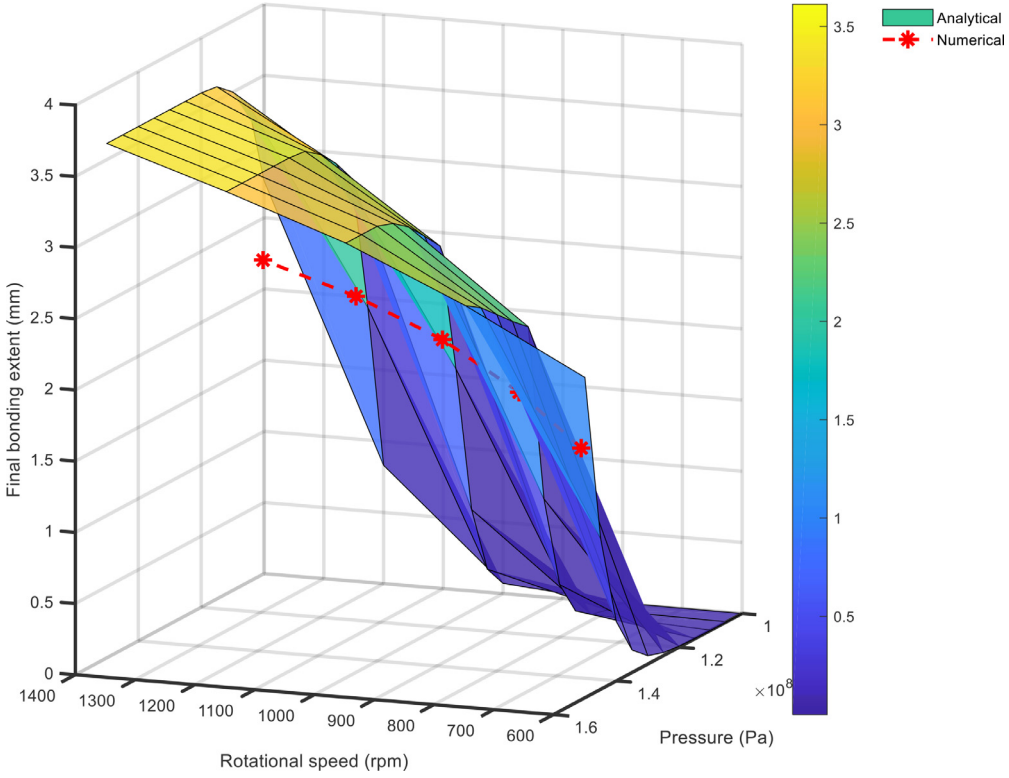

Fig. 19. The final bonding extent on the workpiece-workpiece interface with respect to two processing parameters (axial pressure and tool rotational speed), obtained from the CEL numerical simulations of the FSW setup in Fig. 3(b) and our analytical solution based on Fig. 14.

Declaration of Competing Interest

The authors declare that they have no known competing financial interests or personal relationships that could have appeared to influence the work reported in this paper.

Acknowledgements

The authors would like to acknowledge the financial support of US Army Ground Vehicle Systems Center, made possible through IIP-1540000 and IIP-1822186 from the US National Science Foundation, Industry University Cooperative Research Center (I/UCRC) program, to the University of Tennessee under the Manufacturing and Materials Joining Innovation Center (Ma2JIC). The research is also supported in part from US Department of Energy, Office of Nuclear Energy's Nuclear Energy Enabling Technologies Program, through Oak Ridge National Laboratory, managed by UT-Battelle, LLC, under Contract No. DE-AC05–00OR22725 with the U.S. Department of Energy. YG acknowledges fruitful discussions with C.A. Kocak, H.J. Park, and H. Choo on experimental studies.

Data availability

Data in this work are available upon request to the corresponding authors.

References

[1] F. William, W.L. Horigan Jr., Process for diffusion-bonding, U.S. Patent No. 3,197,858 (1965).
[2] S. Dunkerton, Diffusion bonding – an overview, in: Diffusion Bonding, 2, Springer, 1991, pp. 1–12.
[3] W. Cai, G. Daehn, A. Vivek, J. Li, H. Khan, R.S. Mishra, M. Komarasamy, A state-of-the-art review on solid-state metal joining, J. Manu. Sci. Eng. 141 (2019) 031012.
[4] B. Kang, W. Cai, C.A. Tan, Dynamic response of battery tabs under ultrasonic welding, J. Manu. Sci. Eng. 135 (2013) 051013.
[5] K. Martinsen, S.J. Hu, B.E. Carlson, Joining of dissimilar materials, CIRP Annals 64 (2015) 679–699.
[6] T.Z. Blazynski, Explosive Welding, Forming and Compaction, Springer Science & Business Media, 2012.
[7] A. Loureiro, R. Mendes, J. Ribeiro, R. Leal, I. Galvão, Effect of explosive mixture on quality of explosive welds of copper to aluminum, Mater. Des. 95 (2016) 256–267.
[8] R.S. Mishra, Z.Y. Ma, Friction stir welding and processing, Mater. Sci. Eng. R 50 (2005) 1–78.
[9] R. Nandan, T. DebRoy, H.K.D.H. Bhadeshia, Recent advances in friction-stir welding – Process, weldment structure and properties, Prog. Mater. Sci. 53 (2008) 980–1023.
[10] G. Chen, Z. Feng, Y. Zhu, Q. Shi, An alternative frictional boundary condition for computational fluid dynamics simulation of friction stir welding, J. Mater. Eng. Performance 25 (2016) 4016–4023.
[11] X. Liu, G. Chen, J. Ni, Z. Feng, Computational fluid dynamics modeling on steady-state friction stir welding of aluminum alloy 6061 to TRIP steel, J. Manu. Sci. Eng. 139 (2017) 051004.
[12] X. Wang, Y.F. Gao, X. Liu, M. McDonnell, Z. Feng, Tool-workpiece stick-slip conditions and their effects on torque and heat generation rate in the friction stir welding, Acta Mater 213 (2021) 116969.
[13] Y. Lu, J.Y. Huang, C. Wang, S. Sun, J. Lou, Cold welding of ultrathin gold nanowires, Nature Nanotech 5 (2010) 218–224.
[14] W.T. King, W. Owczarski, Diffusion welding of commercially pure titanium, Weld J 46 (1967) 289.
[15] J.E. Gould, Mechanisms of bonding for solid-state welding processes, in: Welding Fundamentals and Processes, Vol. 6A, ASM Handbook, 2011, pp. 171–178.
[16] C. Hamilton, Pressure requirements for diffusion bonding titanium, in: Titanium Science and Technology, Springer, 1973, pp. 625–648.
[17] G. Chen, Z. Feng, J. Chen, L. Liu, H. Li, Q. Liu, S. Zhang, X. Cao, G. Zhang, Q. Shi, Analytical approach for describing the collapse of surface asperities under compressive stress during rapid solid state bonding, Scripta Mater 128 (2017) 41–44.
[18] Y.F. Gao, A.F. Bower, Elastic-plastic contact of a rough surface with Weierstrass profile, Proc. Roy. Soc. A 462 (2006) 319–348.
[19] S.S. Babu, M.L. Santella, Z. Feng, B.W. Riemer, J.W. Cohron, Empirical model of effects of pressure and temperature on electrical contact resistance of metals, Sci. Tech. Welding Joining 6 (2001) 126–132.
[20] B. Derby, E. Wallach, Theoretical model for diffusion bonding, Metal Sci 16 (1982) 49–56.
[21] B. Derby, E. Wallach, Diffusion bonding: development of theoretical model, Metal Sci 18 (1984) 427–431.
[22] A. Hill, E. Wallach, Modelling solid-state diffusion bonding, Acta Metall 37 (1989) 2425–2437.
[23] Z. Guo, N. Ridley, Modelling of diffusion bonding of metals, Mater. Sci. Tech. 3 (1987) 945–953.
[24] G. Buffa, S. Pellegrino, L. Fratini, Analytical bonding criteria for joint integrity prediction in friction stir welding of aluminum alloys, J. Mater. Process. Technol. 214 (2014) 2102–2111.
[25] A.C.F. Cocks, M.F. Ashby, On creep fracture by void growth, Prog. Mater. Sci. 27 (1982) 189–244.
[26] M.F. Ashby, Mechanisms of deformation and fracture, Adv. Appl. Mech. 23 (1983) 117–177.
[27] V. Tvergaard, Material failure by void growth to coalescence, Adv. Appl. Mech. 27 (1990) 83–151.
[28] W. Zhang, X. Wang, Y. Wang, X. Yu, Y.F. Gao, Z. Feng, Type IV failure in weldment of creep resistant ferritic alloys: I. Micromechanical origin of creep strain localization in the heat affected zone, J. Mech. Phys. Solids 134 (2020) 103774.
[29] W. Zhang, X. Wang, Y. Wang, X. Yu, Y.F. Gao, Z. Feng, Type IV failure in weldment of creep resistant ferritic alloys: II. Creep fracture and lifetime prediction, J. Mech. Phys. Solids 134 (2020) 103775.
[30] W. Zhang, Y.F. Gao, Z. Feng, X. Wang, S. Zhang, L. Huang, Z.W. Huang, L. Jiang, Ductility limit diagrams for superplasticity and forging of high temperature polycrystalline materials, Acta Mater 194 (2020) 378–386.
[31] D. Hull, D. Rimmer, The growth of grain-boundary voids under stress, Phil. Mag. 4 (1959) 673–687.
[32] A. Needleman, J.R. Rice, Plastic creep flow effects in the diffusive cavitation of grain boundaries, Acta Metall 28 (1980) 1315–1332.
[33] X. Wang, Y. Gao, M. McDonnell, Z. Feng, On the solid-state-bonding mechanism in friction stir welding, Extreme Mech. Lett. 37 (2020) 100727.
[34] V. Balasubramanian, Relationship between base metal properties and friction stir welding process parameters, Mater. Sci. Eng. A 480 (2008) 397–403.
[35] A. Esmaeili, H.Z. Rajani, M. Sharbati, M.B. Givi, M. Shamanian, The role of rotation speed on intermetallic compounds formation and mechanical behavior of friction stir welded brass/aluminum 1050 couple, Intermetallics 19 (2011) 1711–1719.
[36] N.R.J. Hynes, P.S. Velu, Effect of rotational speed on Ti-6Al-4V-AA 6061 friction welded joints, J. Manu. Proc. 32 (2018) 288–297.
[37] Z. Shen, Y. Chen, M. Haghshenas, A.P. Gerlich, Role of welding parameters on interfacial bonding in dissimilar steel/aluminum friction stir welds, Eng. Sci. Tech., an Int. J. 18 (2015) 270–277.
[38] M. Boz, A. Kurt, The influence of stirrer geometry on bonding and mechanical properties in friction stir welding process, Mat. Des. 25 (2004) 343–347.
[39] Y.H. Zhao, S.B. Lin, L. Wu, F.X. Qu, The influence of pin geometry on bonding and mechanical properties in friction stir weld 2014 Al alloy, Mater. Lett. 59 (2005) 2948–2952.
[40] T.J. Chuang, J.R. Rice, The shape of intergranular creep cracks growing by surface diffusion, Acta Metall 21 (1973) 1625–1628.
[41] T.J. Chuang, K.I. Kagawa, J.R. Rice, L.B. Sills, Overview no. 2: non-equilibrium models for diffusive cavitation of grain interfaces, Acta Metall 27 (1979) 265–284.
[42] T.-L. Sham, A. Needleman, Effects of triaxial stressing on creep cavitation of grain boundaries, Acta Metall 31 (1983) 919–926.
[43] H.J. Frost, M.F. Ashby, Deformation Mechanism Maps: the Plasticity and Creep of Metals and Ceramics, Pergamon Press, 1982.
[44] T. Sheppard, A. Jackson, Constitutive equations for use in prediction of flow stress during extrusion of aluminum alloys, Mater. Sci. Tech. 13 (1997) 203–209.
[45] R. Crawford, G. Cook, A. Strauss, D. Hartman, M. Stremler, Experimental defect analysis and force prediction simulation of high weld pitch friction stir welding, Sci. Tech. Welding Joining 11 (2006) 657–665.
[46] F. Al-Badour, N. Merah, A. Shuaib, A. Bazoune, Coupled Eulerian Lagrangian finite element modeling of friction stir welding processes, J. Mater. Proc. Tech. 213 (2013) 1433–1439.
[47] Y. Chao, S. Liu, C.H. Chien, Friction stir welding of al 6061-T6 thick plates: Part II-numerical modeling of the thermal and heat transfer phenomena, J. Chin. Inst. Eng. 3 (2008) 769–779.
[48] R. Hill, Similarity analysis of creep indentation tests, Proc. Roy. Soc. London A 436 (1992) 617–630.
[49] A.F. Bower, N.A. Fleck, A. Needleman, N. Ogbonna, Indentation of a power law creeping solid, Proc. Roy. Soc. London A 441 (1993) 97–124.
[50] J.H. Lee, Y.F. Gao, A.F. Bower, H.T. Xu, G.M. Pharr, Stiffness of frictional contact of dissimilar elastic solids, J. Mech. Phys. Solids 112 (2018) 318–333.
[51] K.L. Johnson, Contact Mechanics, Cambridge University Press, 1985.
[52] D. Rosenthal, Mathematical theory of heat distribution during welding and cutting, Welding J 20 (1941) 220–234.
[53] B. Panda, A. Garg, Z. Jian, A. Heidarzabeh, L. Gao, Characterization of the tensile properties of friction stir welded aluminum alloy joints based on axial force, traverse speed, and rotational speed, Front. Mech. Eng. 11 (2016) 289–298.
[54] H.J. Park, H. Choo, private discussions.